Article

Developmental Cell

Organoid modeling of lung branching morphogenesis and epithelial lineage specification

Graphical abstract

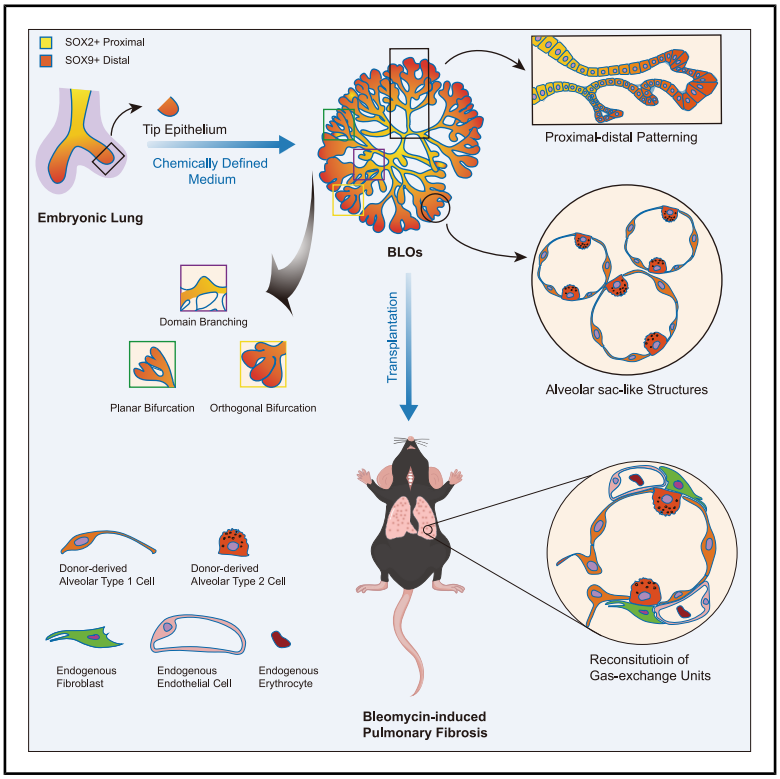

Highlights

- A chemically defined culture system generates multilevel branching lung organoids (BLOs)
- BLOs recapitulate proximodistal patterning and lung epithelial lineage specification
- Live imaging reveals branching dynamics of BLOs
- BLO-derived cells engraft injured lungs and ameliorate bleomycin-induced fibrosis

Authors

Mengjie Pan, Baomei Cai, Guanlie Li, ..., Man Zhang, Mingwei Min, Shangtao Cao

Correspondence

gong_an@gzlab.ac.cn (A.G.), peiduanqing@westlake.edu.cn (D.P.), chen_jiekai@gibh.ac.cn (J.C.), zhang_man@gzlab.ac.cn (M.Z.), min_mingwei@gzlab.ac.cn (M.M.), cao_shangtao@gzlab.ac.cn (S.C.)

In brief

Pan et al. establish branching lung organoids (BLOs) using a chemically defined culture system. BLOs recapitulate proximodistal patterning, epithelial lineage progression, and branching dynamics of the developing lung, whereas BLO-derived cells engraft injured lungs and promote alveolar regeneration after fibrotic injury.

Pan et al., 2026, Developmental Cell *61*, 1504–1520
July 8, 2026
https://doi.org/10.1016/j.devcel.2026.05.012

CellPress

CellPress
OPEN ACCESS

Developmental Cell

Article

Organoid modeling of lung branching morphogenesis and epithelial lineage specification

Mengjie Pan,[1,2,7] Baomei Cai,[1,2,7] Guanlie Li,[1,2,7] Ruifang Zhang,[1,2,7] Chuncao Deng,[1,5,7] Huan Chen,[1,2,7] Yingxiu Chen,[1,2] Sihao Chen,[1] Ziyu Feng,[1,2] Xiongzhi Quan,[3] Yunjing Du,[2] Wei He,[1,2] Yiyi Cheng,[1,2] Chunhua Zhou,[1,2] Yudong Fu,[1,2] Shujuan Liu,[1,4] Dafeng Tao,[1,2] Yangqing Tian,[1,2] Jiajun Hou,[1,2] Yongchang Huang,[1,2] Yiwei Li,[5] Shengyong Yu,[1] Dajiang Qin,[1,4] An Gong,[1,2,*] Duanqing Pei,[6,*] Jiekai Chen,[3,*] Man Zhang,[1,2,*] Mingwei Min,[1,2,*] and Shangtao Cao[1,2,8,*]

[1]Guangzhou National Laboratory, The Fifth Affiliated Hospital of Guangzhou Medical University, Guangzhou, Guangdong 510005, China
[2]Guangzhou National Laboratory, Guangzhou International Bio Island, Guangzhou, Guangdong 510005, China
[3]Center for Biomedical Digital Science, Guangdong Provincial Key Laboratory of Stem Cell and Regenerative Medicine, Guangzhou Institutes of Biomedicine and Health, Chinese Academy of Sciences, Guangzhou, Guangdong 510530, China
[4]Key Laboratory of Biological Targeting Diagnosis, Therapy and Rehabilitation of Guangdong Higher Education Institute, The Fifth Affiliated Hospital of Guangzhou Medical University, Guangzhou, Guangdong 510700, China
[5]Department of Biomedical Engineering, College of Life Science and Technology, Huazhong University of Science and Technology, Wuhan, Hubei 430074, China
[6]Laboratory of Cell Fate Control, School of Life Sciences, Westlake University, Hangzhou, Zhejiang 310030, China
[7]These authors contributed equally
[8]Lead contact
*Correspondence: gong_an@gzlab.ac.cn (A.G.), peiduanqing@westlake.edu.cn (D.P.), chen_jiekai@gibh.ac.cn (J.C.), zhang_man@gzlab.ac.cn (M.Z.), min_mingwei@gzlab.ac.cn (M.M.), cao_shangtao@gzlab.ac.cn (S.C.)
https://doi.org/10.1016/j.devcel.2026.05.012

SUMMARY

Branching morphogenesis is a fundamental process governing pulmonary development, epithelial differentiation, and functional maturation. Here, we report a multilevel branching lung organoid (BLO) model generated from primary tip epithelial cells using a robust, chemically defined protocol. These BLOs exhibit characteristic dendritic architectures with proximodistal patterning and alveolar-sac-like structures. Time-resolved single-cell RNA sequencing reveals that BLOs comprise both proximal airway and distal alveolar epithelial populations and recapitulate the developmental trajectories of lung epithelial lineages *in vitro*. Live-cell imaging further demonstrates that the spatial organization and branching dynamics of BLOs closely resemble those of native murine pulmonary epithelium *in vivo*. Upon transplantation into bleomycin-injured murine models, BLO-derived cells further mature and ameliorate pulmonary fibrosis. Together, these findings establish BLOs as a powerful platform for investigating lung branching morphogenesis, epithelial lineage specification and regeneration.

INTRODUCTION

Organoid technology provides a promising *in vitro* platform for modeling tissue development, regeneration, and disease by reconstructing organ-specific cell lineages in three dimensions.[1] To date, although organoids have been established for multiple organs,[1,2] including lung, intestine, liver, and brain, most epithelial organoids remain structurally simplistic. They typically form spherical cysts lacking higher-order spatial organization, making it difficult to infer tissue identity and model tissue morphogenesis and developmental patterning.

This limitation is particularly evident in lung organoid systems. Current airway and alveolar organoids fail to recapitulate the highly ordered branched architecture of the pulmonary epithelium.[3–11] Recent studies have shown that lung bud organoids derived from pluripotent stem cells (PSCs) can exhibit branching-like morphologies[12]; however, these structures display disorganized branching patterns and poorly regionalized epithelial cell types *in vitro*. Moreover, off-target lineages, such as gut epithelium, frequently arise during PSC differentiation, further limiting their utility.[13] Consequently, current lung organoid models remain constrained in their ability to faithfully model lung development, particularly with respect to recapitulating the ordered branched architecture of the pulmonary epithelium. In parallel, advances in PSC differentiation and 3D culture systems have enabled the generation of embryo-like structures that mimic early developmental events, including blastocyst formation and gastrulation.[14–17] While powerful, these systems generally fail to progress beyond pre-organogenesis stages. Thus, alternative strategies are required to reconstruct lung

CellPress
OPEN ACCESS

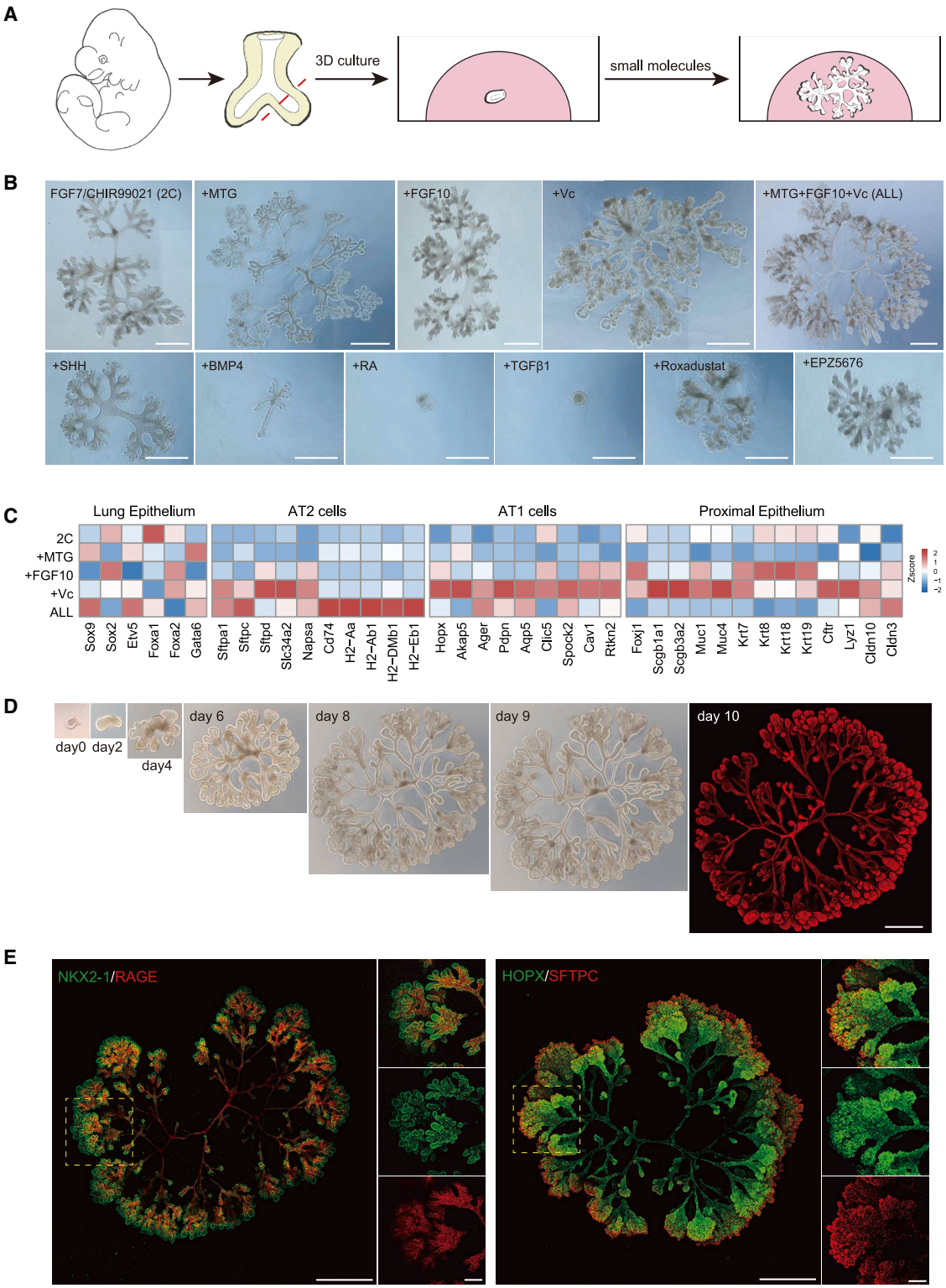

Figure 1. Generation and characterization of BLOs from E10.5 lung tip epithelium

(A) Schematic overview of the strategy used to generate BLOs.

(B) Bright-field images comparing branching morphogenesis under the 2C condition, 2C supplemented with single factor, and the optimized "ALL" condition, in which 2C is combined with MTG, FGF10, and Vc. Top row, montages; bottom row, single-field images. Scale bars, 500 μm.

(C) Heatmap showing the expression of lung epithelial lineage markers across different culture conditions.

(legend continued on next page)

morphogenetic programs such as branching morphogenesis to enable precise modeling of epithelial fate decisions and regeneration.

Branching morphogenesis is a defining feature of lung development, establishing the dendritic architecture required for subsequent epithelial differentiation and functional maturation.[18,19] In the mouse, lung branching initiates around embryonic day (E) 10.5, when the lung primordium bifurcates into left and right buds and undergoes iterative branching to generate a stereotyped dendritic architecture with defined proximodistal patterning, giving rise to four lobes in the right lung and a single lobe in the left lung.[20] This process is governed by coordinated epithelial-mesenchymal signaling, with pathways such as fibroblast growth factor (FGF), Wnt, and bone morphogentic protein (BMP)/transforming growth factor β (TGF-β) playing essential roles.[21–23] Disruption of key regulators, including FGF10 or fibroblast growth factor receptor 2 (FGFR2), results in severe branching defects,[24,25] highlighting the importance of accurately modeling this process.

Here, we establish branching lung organoids (BLOs) that recapitulate multilevel branching morphogenesis, epithelial lineage specification, and alveolar maturation, providing a versatile platform for studying lung development and regeneration.

RESULTS

Generation of BLOs from E10.5 lung tip epithelium under chemically defined conditions

Current lung organoid systems typically form simple spherical structures and fail to recapitulate the branched architecture of the lung *in vivo*. These limitations arise largely from inappropriate cell sources and the use of undefined culture components. Adult lung epithelial cells exhibit restricted differentiation capacity, whereas PSC-derived lung epithelium often diverges from native developmental states. In addition, undefined components such as serum may interfere with morphogenetic programs required for branching.[26] We therefore hypothesized that both the developmental identity of the starting epithelial population and precise control of culture conditions are critical for establishing multilevel BLOs *in vitro*. To test this, embryonic lung buds were isolated from E10.5 institute of cancer research (ICR) mouse embryos, and stromal cells were removed to obtain epithelial tip fragments. These fragments were embedded in Matrigel and cultured under chemically defined conditions (Figure 1A).

We first performed a systematic screen of small molecules and growth factors involved in signaling pathways known to regulate lung branching morphogenesis and epithelial fate specification (Table S1). Among the tested factors, only the FGF signaling agonist FGF7 promoted epithelial tip proliferation, whereas other factors either had minimal effects or induced apoptosis (Figure S1A). Based on this result, a second round of screening was conducted in the presence of FGF7. We found that the Wnt signaling agonist CHIR99021 synergized with FGF7 to enhance epithelial expansion and induce branching morphologies (Figure 1B).

We next evaluated additional factors in combination with FGF7 and CHIR99021. Monothioglycerol (MTG), vitamin C (Vc), and FGF10 further improved branching complexity (Figure 1B) and epithelial differentiation (Figure 1C), whereas BMP4, TGF-β1, retinoic acid (RA), roxadustat, and EPZ5676 inhibited branching (Figure 1B). Compared with treatment using FGF7 and CHIR99021 alone, the addition of FGF10, Vc, and MTG together enhanced multilevel branching and pulmonary epithelial lineage differentiation (Figures 1B and 1C). Based on these results, we established a chemically defined medium consisting of five components: CHIR99021, FGF7, FGF10, Vc, and MTG.

Under these conditions, lung epithelial tips exhibited progressive growth and expansion. By day 4, pronounced epithelial budding and branching were evident. With prolonged culture, the organoids continued to generate higher-order branches, with terminal regions expanding into alveolar-sac-like structures (Figure 1D). In contrast, BMP4, RA, and epidermal growth factor (EGF), which were included in previously reported lung branching organoid systems,[12] failed to enhance branching and disrupted branching in our system (Figure S1B). We therefore termed these structures branching lung organoids (BLOs), reflecting their characteristic dendritic architecture.

To characterize the molecular identity of BLOs, we performed whole-mount immunofluorescence analysis. BLOs uniformly expressed the lung lineage marker NKX2-1, as well as alveolar epithelial markers including SFTPC, HOPX, and RAGE, confirming their pulmonary epithelial identity (Figure 1E). Given the distal tip origin of BLOs, we further examined whether proximodistal patterning emerged during organoid development. Time-course analyses were performed on BLOs collected at days 2, 4, 6, 8, and 11 using whole-mount and sectioned immunofluorescence staining. The proximal airway marker SOX2 and distal epithelial marker SOX9 displayed distinct and spatially segregated expression patterns, with SOX2 enriched in central regions and SOX9 localized to distal branching tips (Figures 2A and 2B). SOX2 expression was initiated by day 2, progressively increased through day 8, and subsequently decreased by day 11, indicating the establishment and maintenance of proximodistal patterning followed by epithelial lineage differentiation. ICAM1$^+$ transitional cells[27] were detected at the interface between SOX2$^+$ and SOX9$^+$ regions (Figures 2A and 2B). Distal alveolar markers were activated in a staged manner, with HOPX and SFTPC emerging after day 4 (Figure S1C). Distal alveolar-sac-like structures contained both alveolar type 1 (AT1) and type 2 (AT2) cells, with AT1 cells exhibiting flattened morphologies and AT2 cells interspersed between AT1 cells (Figures 2C and S1C). Consistent with these observations, bulk RNA sequencing (RNA-seq) revealed progressive differentiation of BLO-derived cells from distal progenitors toward AT2 and AT1 fates, accompanied by a marked enrichment of mature AT2- and AT1-associated gene signatures at later stages of culture (Figure 2D).

(D) Representative images of BLOs from days 0 to 9, together with a live fluorescence image of a day−10 organoid stained for F-actin. Days 8–10, montages. Scale bar, 500 μm.

(E) Representative whole-mount immunofluorescence images of day 13 BLOs stained for NKX2-1, SFTPC, HOPX, and RAGE. Left panels (montages) show whole-organoid views, and right panels show higher-magnification images of boxed regions. Scale bars, 500 (left) and 100 μm (right).

See also Figure S1.

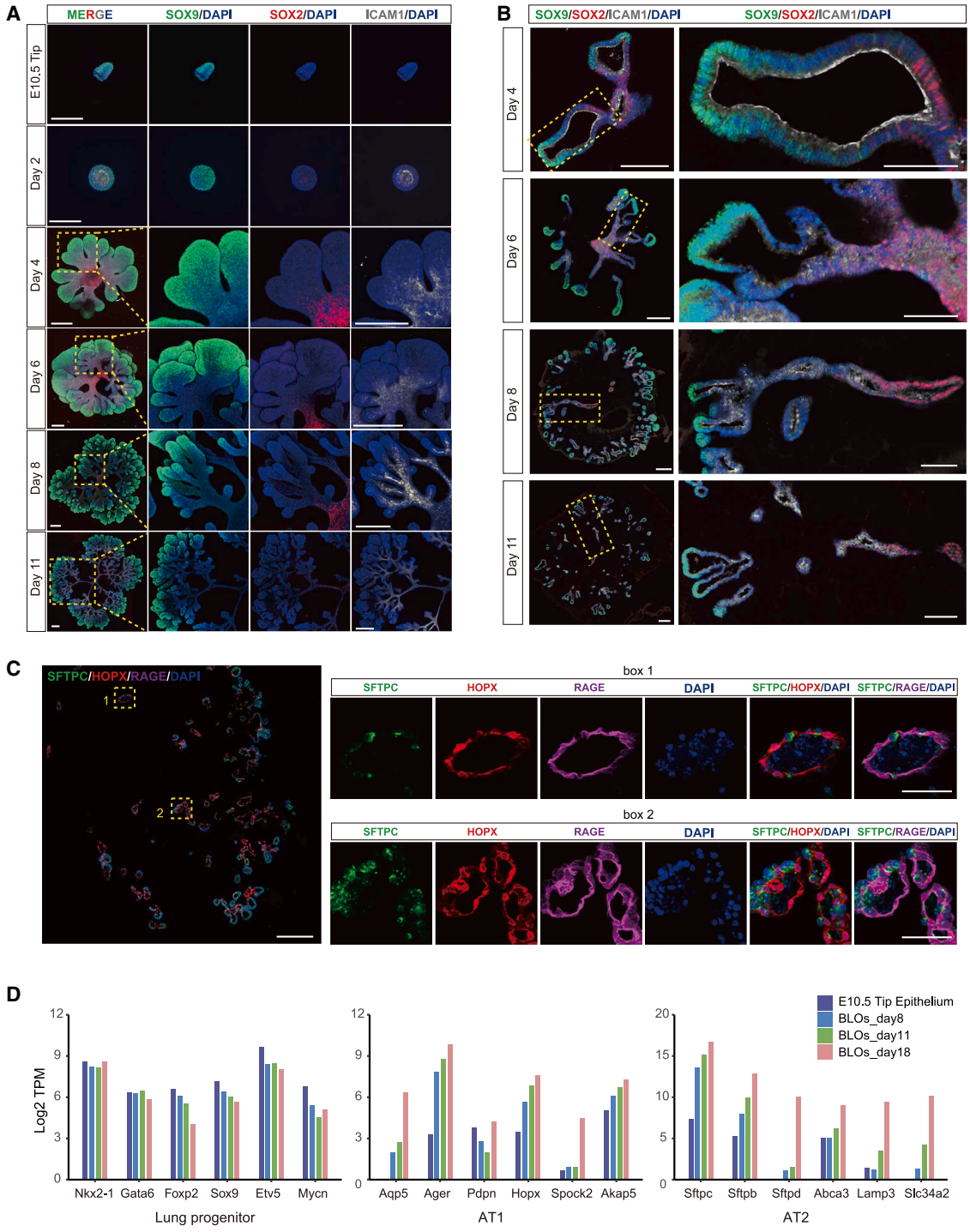

Figure 2. BLOs recapitulate proximal-distal patterning and lineage progression

(A) Whole-mount immunofluorescence analysis of BLOs at days 2, 4, 6, 8, and 11, and of E10.5 lung tips, stained for SOX9, SOX2, and ICAM1. Days 8 and 11 are montages. For days 4–11, higher-magnification views of boxed regions are shown on the right. Scale bars, 200 μm.

(B) BLO sections at days 4, 6, 8, and 11 stained for the same marker as in (A). Days 8 and 11 are montages. Yellow dashed boxes indicate regions shown at higher magnification in the right panels. Scale bars, 200 μm (left) and 100 μm (right).

(C) Immunofluorescence staining of day 18 BLO section for SFTPC, HOPX, and RAGE. The image is a montage. Right panels show higher-magnification views of boxed regions 1 and 2. Scale bars, 200 (left) and 50 μm (right).

(D) Gene expression dynamics of BLOs at days 8, 11, and 18.

See also Figure S1.

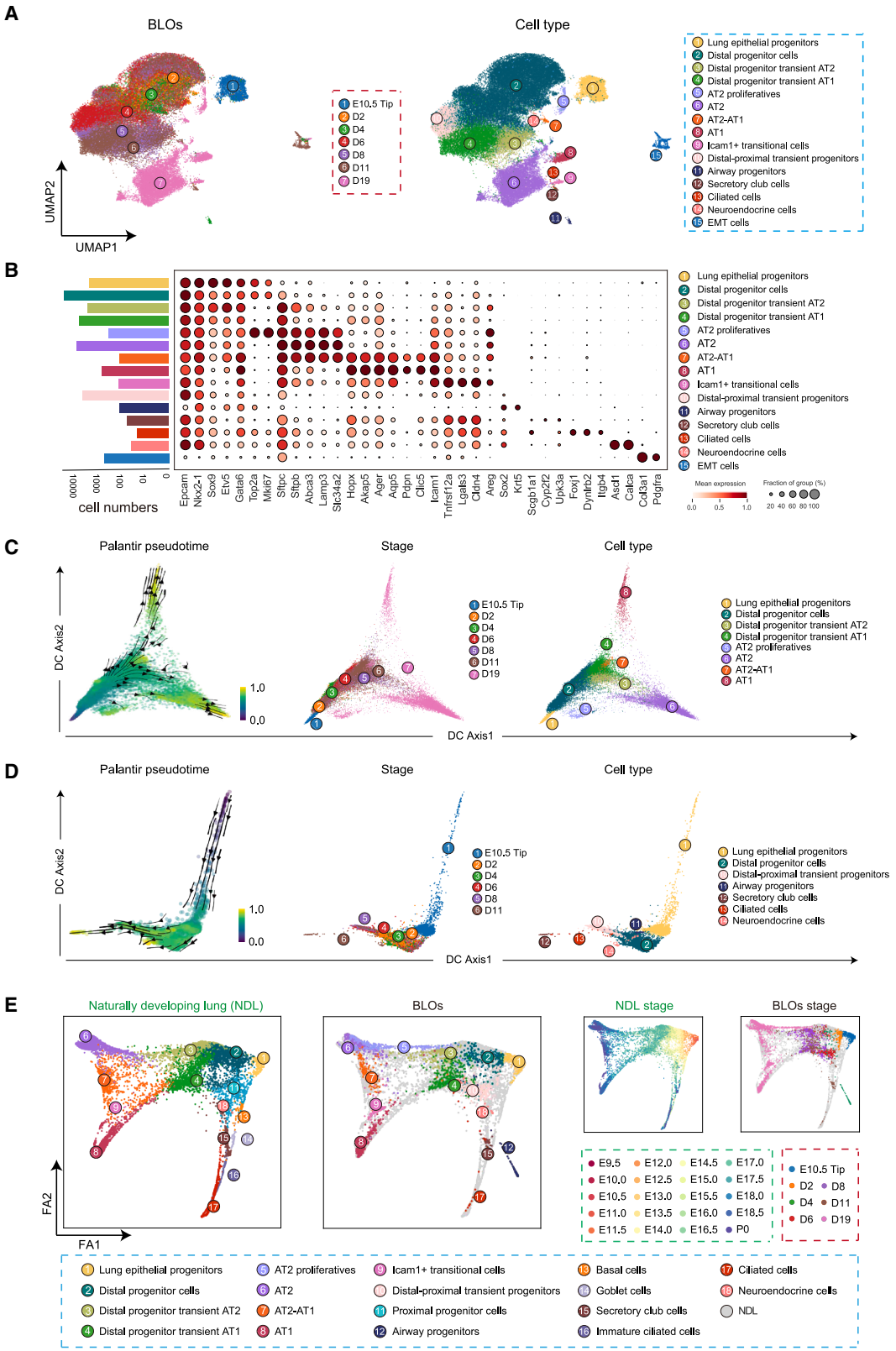

Figure 3. BLOs reconstruct lung epithelial developmental lineages *in vitro*

(A) UMAP visualization of single-cell transcriptomes from BLOs.

(B) Bar plots showing the number of cells in each identified cell type (left). Dot plot depicting the expression of representative genes across BLO cell types (right).

(legend continued on next page)

Together, these results indicate that BLOs undergo coordinated multilevel branching and proximodistal patterning and generate regionally organized proximal and distal epithelial cells, closely recapitulating features of native lung development.

BLOs reconstruct lung epithelial developmental lineages *in vitro*

Given that BLOs are derived from early lung buds and undergo proximodistal patterning, we examined whether BLOs recapitulate lung epithelial developmental trajectories *in vitro*. To this end, we performed single-cell RNA-seq (scRNA-seq) on BLOs collected at days 2, 4, 6, 8, 11, and 19 of culture, together with E10.5 lung tips as a developmental reference (Figure 3A). This analysis yielded high-quality transcriptomes from 57,150 cells, with a median of 3,448 genes and 13,508 unique molecular identifiers (UMIs) detected per cell (Figure S2A). Uniform manifold approximation and projection (UMAP) analysis revealed diverse epithelial populations across successive stages of culture. Early-stage BLOs (days 2–11) were enriched for distal progenitors, transient progenitors, immature alveolar cells, and proximal airway progenitors, as well as differentiated proximal airway lineages including club, ciliated, and neuroendocrine cells. In contrast, late-stage BLOs (day 19) were predominantly composed of mature AT1 and AT2 cell populations (Figures 3A and 3B). Cells committed to distal epithelial fates constituted the majority of the BLO population throughout culture, whereas proximal airway lineages represented a smaller fraction (Figure 3B). With extended culture, distal lineages exhibited progressive maturation, accompanied by a further reduction in proximal populations, indicating that the defined culture conditions preferentially support distal epithelial specification.

Developmental trajectory analysis of distal lineages revealed a continuous differentiation pathway from distal progenitors to AT2 and subsequently AT1 cell fates (Figure 3C). This process was accompanied by a progressive enrichment of mature AT1 populations at later culture stages, consistent with the immunofluorescence findings previously described (Figure 2C). Concurrently, trajectory analysis of proximal lineages demonstrated a differentiation process from distal progenitors into proximal airway progenitors and their downstream epithelial derivatives (Figure 3D). These observations indicate that BLOs undergo distal-to-proximal lineage specification during branching morphogenesis.

To assess the fidelity of BLOs relative to native lung development, we compared BLO transcriptomes with a mouse lung epithelial developmental atlas spanning E9.5 through the neonatal stage (Figure S2B).[28] Trajectory alignment revealed that BLO differentiation paths closely mirrored those observed *in vivo*, with comparable distributions of distal and proximal epithelial populations (Figure 3E). Correlation analysis demonstrated strong transcriptional similarity between corresponding cell types in BLOs and fetal or post-natal lungs (Figure S2C). Principal-component analysis (PCA) further positioned BLOs along the developmental timeline, with day 19 BLOs aligning closely with E17.5 mouse lungs (Figure S2D). Moreover, consistent with *in vivo* signal response,[29] treatment of BLOs with dexamethasone, cyclic AMP (cAMP), and isobutylmethylxanthine (DCI) accelerated alveolar epithelial maturation, and upregulated AT2 and AT1 marker genes (Figures S2E and S2F). Immunofluorescence analysis showed that SFTPC expression transitioned from a broad distribution to a more restricted pattern localized to AT2 cells. Under DCI treatment, BLOs more readily formed alveolar-sac-like structures compared with control conditions (Figure S2G).

Together, these results demonstrate that BLOs reconstruct lung epithelial developmental lineages *in vitro*, providing a temporally resolved platform for studying pulmonary development and maturation.

Branching dynamics of BLOs

We next characterized the branching dynamics of BLOs. Using bright-field time-lapse microscopy, we tracked BLO growth over the first 5 days of culture. During early development, BLOs exhibited two distinct growth modes. Type-I organoids remained quiescent for the first 1–2 days before entering a rapid expansion phase preceding bud initiation (Figures 4A and S3A), whereas type-II organoids grew at a near-constant rate and initiated budding significantly earlier (Figures 4B, 4C, and S3B). Notably, both types reached comparable sizes at the onset of budding (Figure 4D), suggesting the existence of a size-dependent threshold for bud initiation.

By day 5, BLOs formed higher-order branched architectures (Figure 4E). Consistent with mammalian lung development, which proceeds through three canonical branching modes—domain branching, planar bifurcation, and orthogonal bifurcation—BLOs exhibited all three patterns (Video S1). Among these, planar bifurcation was the most frequent, followed by domain branching and orthogonal bifurcation (Figure 4F).

To quantitatively compare BLO branching architectures with those of *in vivo* lungs, we developed a branching kernel composition vector (BKCV), a scalable tree-embedding framework. We defined two fundamental branching events as level-1 (L1) kernels—budding (branching) and clefting (bifurcation). Level-2 (L2) kernels consist of two connected L1 kernels. After emulating all possible non-isomorphic L2 kernels, we constructed a branching kernel atlas (Figures 4G and S3C). Each branching tree was then represented as a BKCV, encoding the relative frequencies of individual L2 kernel types (Figures 4G and S3C).

Dimensionality reduction of BKCVs using UMAP revealed that branching tree development maps onto a continuous trajectory in low-dimensional space (Figure 4H). To validate this concept, we sequentially pruned thinnest branches from adult mouse airway trees until a certain number of nodes remained to simulate the mouse airway at different development stages (Figure S3D). Indeed, this generated a continuous putative developmental trajectory. Mouse and human lungs occupied distinct regions of the UMAP space, indicating species-specific branching programs, and were clearly separated from another branched

(C and D) Differentiation trajectory analysis of distal (C) and proximal (D) lineages. DC, diffusion component.
(E) Force-directed graph layouts (ForceAtlas2 [FA]) integrating BLOs with naturally developing lung (NDL) datasets spanning E9.5 to P0. Left panels show the distribution of cell types in NDL (left) and BLOs (right). Right panels depict the alignment of developmental stages between NDL (left) and BLOs (right).
See also Figure S2.

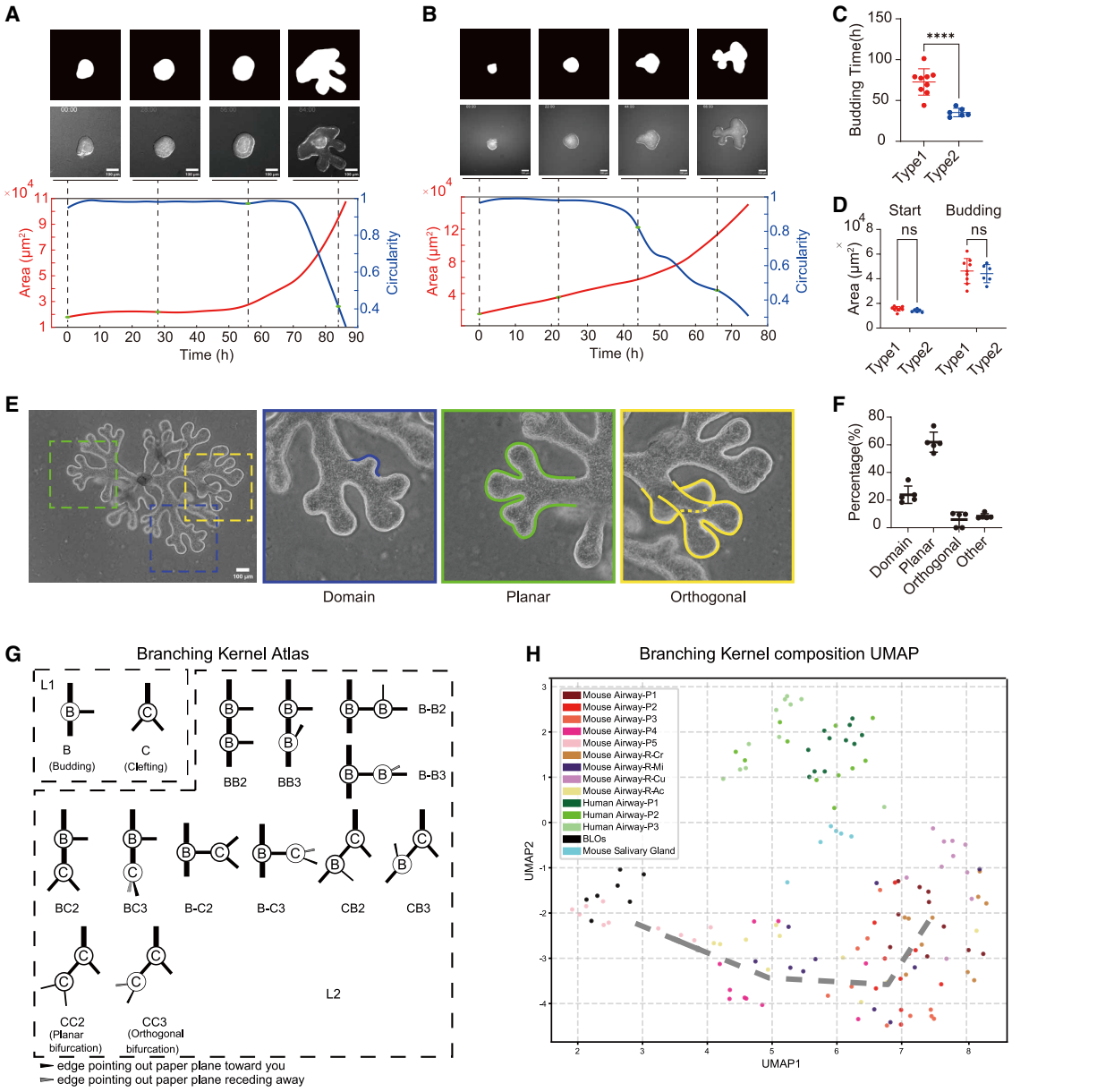

Figure 4. Branching dynamics of BLOs

(A and B) Distinct growth and budding behaviors of type 1 (A) and type 2 (B) BLOs. Top, segmentation masks used for quantitative analysis; middle, representative time-lapse image montages; bottom, quantification of organoid area and circularity over time for representative BLOs of each type. Scale bars, 100 μm.

(C) Quantification of budding onset time in type 1 and type 2 BLOs ($n = 6$ for type 1; $n = 9$ for type 2). Dots represent individual BLOs. Error bars indicate mean ± SD. $p < 0.0001$ by Welch's t test.

(D) Area at starting point and at budding in two types of organoids in type 1 and type 2 BLOs ($n = 6$ for type 1; $n = 9$ for type 2). Dots represent individual BLOs. Error bars indicate mean ± SD. $p > 0.05$ by unpaired t test.

(E) Bright-field image of a representative day-6 BLO illustrating three distinct branching modes within a single organoid. Scale bar, 100 μm.

(F) Quantification of the relative frequencies of three branching modes observed in day 6 BLOs ($n = 5$). Dots represent individual BLOs. Error bars indicate mean ± SD.

(G) Schematic illustration of the branching kernel atlas.

(H) UMAP visualization of BKCVs derived from mouse airway, human airway, mouse salivary gland, and BLOs datasets. R-Cr, right cranial lobe; R-Mi, right middle lobe; R-Cu, right caudal lobe; R-Ac, right accessory lobe. Dashed line indicates the inferred trajectory of mouse airway development.

See also Figure S3.

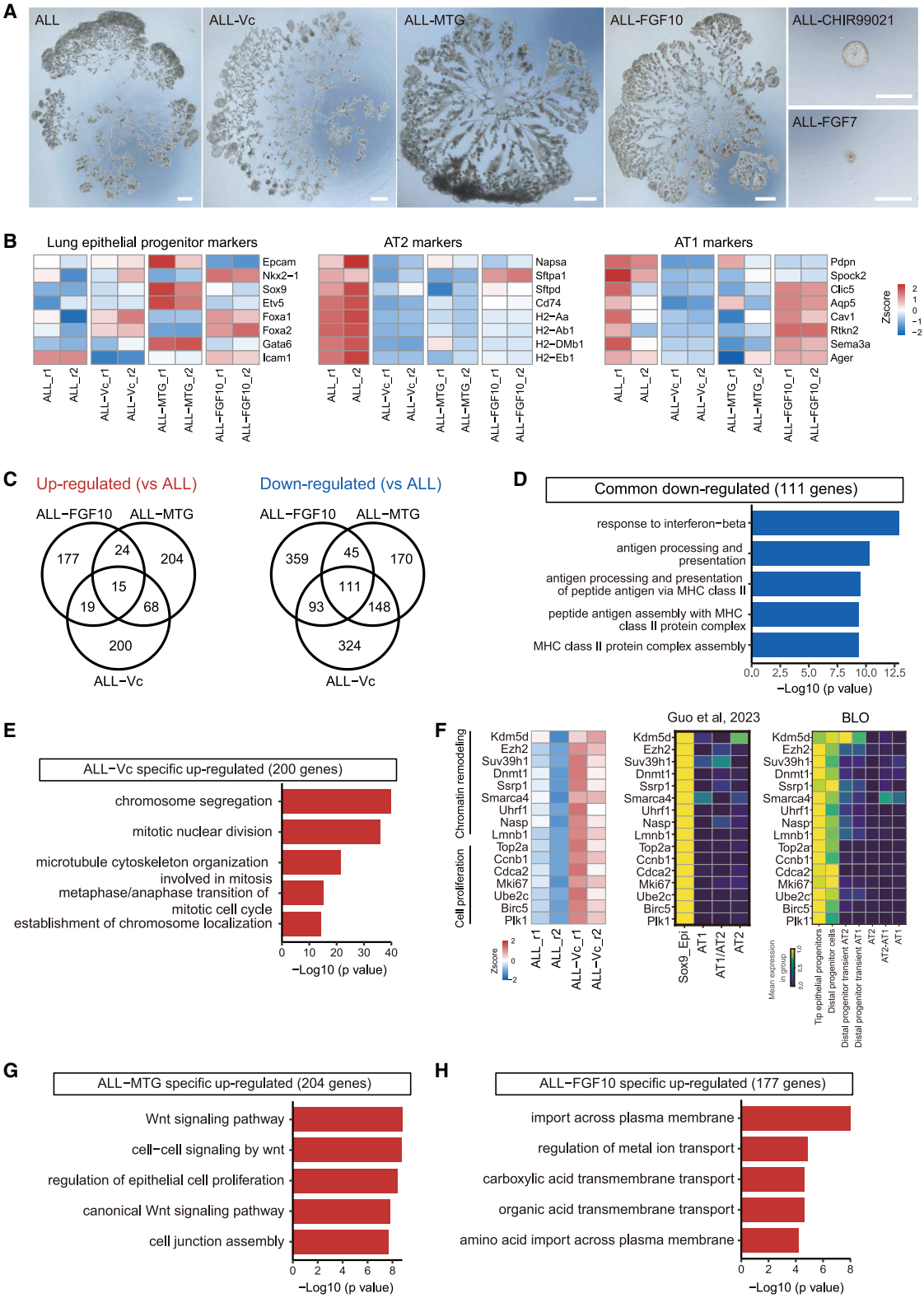

Figure 5. Individual components of the chemical cocktail are indispensable for BLO induction and lineage differentiation

(A) Representative images of organoids cultured under indicated conditions. Organoids were derived from E10.5 lung tips and cultured under ALL, ALL-Vc, ALL-MTG, or ALL-FGF10 conditions for 21 days (montage), or under ALL-CHIR or ALL-FGF7 conditions for 7 days. Scale bars, 500 μm.

(B) Heatmap showing the expression of lung epithelial progenitor, AT2, and AT1 markers in cells under indicated conditions.

(legend continued on next page)

organ, the salivary gland. Strikingly, BLOs clustered closely with mouse lung trees, particularly those corresponding to early developmental stages (Figure 4H). Together, these analyses demonstrate that BLOs faithfully recapitulate the dynamic branching behaviors and architectural features of *in vivo* lung morphogenesis.

Essential factors governing BLO formation

Lung branching morphogenesis is orchestrated by both extrinsic cues from the surrounding environment and intrinsic properties of the cells.[19] To define the essential components required for BLO formation in our culture system, we systematically omitted individual small molecules from the induction medium. Among all conditions tested, withdrawal of the Wnt agonist CHIR99021 or FGF7 produced the most severe phenotypes. In both cases, branching morphogenesis was completely abolished, and the lung bud tip epithelium formed only small, cystic organoids, indicating a failure to initiate bud outgrowth and proliferation (Figure 5A). These findings demonstrate that CHIR99021 and FGF7 are indispensable for BLO initiation and early morphogenetic expansion.

Removal of other small molecules, including FGF10, Vc, or MTG, also compromised branching features of BLOs, albeit to varying extents (Figure 5A). To assess the molecular consequences of these perturbations, we performed bulk RNA-seq on BLOs cultured under each dropout condition. Across all conditions, omission of any single component led to increased expression of distal lung epithelial progenitor markers, including *Sox9*, *Etv5*, *Gata6*, and *Foxa2*, concomitant with reduced expression of alveolar epithelial maturation genes. These included AT2 cell markers (*Sftpa1*, *Sftpd*, *Napsa*, and major histocompatibility complex class II [MHC class II]-complex-related genes) and AT1 cell markers (*Pdpn* and *Spock2*), indicating impaired lineage maturation (Figure 5B).

Comparative transcriptomic analyses revealed both shared and component-specific transcriptional responses (Figure 5C). Genes commonly downregulated upon withdrawal of FGF10, MTG, or Vc were significantly enriched for pathways related to MHC class II complex assembly and antigen presentation (Figure 5D), whereas the number of genes commonly upregulated across all conditions was minimal. In contrast, removal of each component led to the induction of a substantial and largely distinct set of uniquely upregulated genes (Figure 5C), indicating that these factors act through partially overlapping yet mechanistically divergent regulatory programs.

Notably, Vc withdrawal elicited a pronounced and distinctive transcriptional response. Genes specifically upregulated under this condition were strongly enriched for pathways involved in cell-cycle regulation and chromatin remodeling (Figure 5E), including *Kdm5d*, *Ezh2*, *Suv39h1*, *Dnmt1*, *Smarca4*, and *Ssrp1* (Figure 5F). These genes are highly expressed in distal lung progenitors but are normally downregulated during AT1 and AT2 maturation (Figure 5F). Among them, *Suv39h1* has been reported to suppress surfactant gene expression in the fetal lung,[31] while Dnmt1 is required for proper proximodistal patterning and restriction of AT2 cell fate.[32] Our previous work demonstrated that Vc enhances somatic cell reprogramming through epigenetic mechanisms, including modulation of histone modifications[33] and DNA methylation.[34] These findings suggest that Vc promotes BLO morphogenesis and functional maturation, at least in part, by facilitating appropriate epigenetic state transitions. By comparison, genes uniquely upregulated upon MTG withdrawal were enriched for pathways associated with Wnt signaling and regulation of epithelial cell migration (Figure 5G), whereas genes specifically induced by FGF10 withdrawal were primarily related to transmembrane transport processes (Figure 5H).

In addition to chemical cues, we next asked whether the intact spatial organization of lung bud tip epithelium is required for BLO formation. To address this, we dissected tip epithelium into smaller clusters and embedded them in Matrigel under the same induction conditions used for intact tissue. Remarkably, all epithelial clusters generated multilevel branching structures comparable to those derived from intact tip epithelium (Figure S4A). To further characterize these structures, we performed RNA-seq on BLOs derived from epithelial clusters. Transcriptomic analyses revealed a high degree of correlation between samples (Figure S4B), with significant enrichment of genes involved in lung epithelial branching and alveolar development (Figures S4C and S4D). These findings demonstrate that BLO formation does not depend on the intact spatial architecture of the starting tissue, highlighting an intrinsic self-organizing capacity of lung epithelial clusters under defined culture conditions.

The intrinsic branching potential of lung tip epithelium prompted us to examine whether BLO formation is conserved across genetic backgrounds and developmental stages. Tip epithelium isolated from E10.5 C57BL/6 embryos generated BLOs with characteristic branching morphologies, indistinguishable from those derived from ICR mice (Figures 6A and S5A). This indicates that the BLO induction system is reproducible across mouse strains.

To assess developmental competence, we isolated lung bud tip epithelium or distal epithelial clusters from embryos spanning E9.5–E18.0 and subjected them to 3D culture. Tip epithelium isolated between E9.5 and E12.0 exhibited a 100% efficiency in forming multilevel branched structures (Figures 6A, 6C, and S5A), comparable to E10.5-derived BLOs. In contrast, branching efficiency progressively declined from E12.5 onward, dropping to approximately 20% by E14.0 (Figure 6C). Tip or distal epithelium isolated after E14.5 lost the capacity for branching morphogenesis and instead formed simple cystic organoids (Figure 6B).

(C) Venn diagrams depicting the numbers of overlapping upregulated (left) and downregulated (right) genes in ALL-Vc, ALL-MTG, or ALL-FGF10 conditions compared with the ALL condition.
(D) Gene Ontology (GO) term enrichment analysis of the commonly downregulated genes shown in (C) (right).
(E) GO term enrichment analysis of genes uniquely upregulated under the ALL-Vc condition shown in (C) (left).
(F) Heatmap showing the expression of genes associated with cell proliferation and chromatin remodeling across ALL and ALL-Vc conditions (left), mouse lung reference cells from Guo et al., 2023[30] (middle), and BLO-derived cell populations (right).
(G) GO term enrichment analysis of genes uniquely upregulated under ALL-MTG condition shown in (C) (left).
(H) GO term enrichment analysis of genes uniquely upregulated under ALL-FGF10 condition shown in (C) (left).
See also Figure S4.

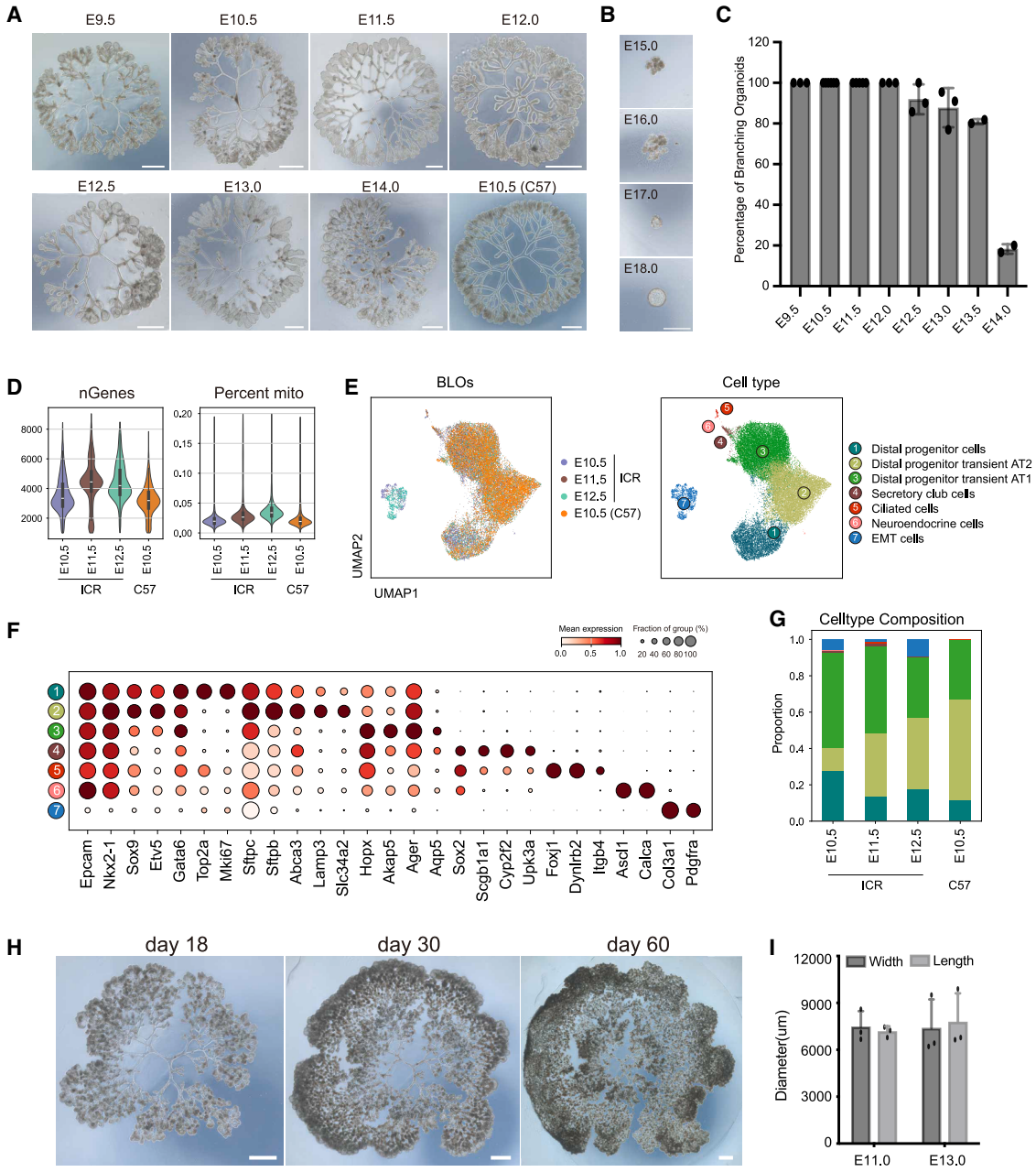

Figure 6. Comparable features of BLOs derived from E9.5 to E14.0 lung tip epithelium

(A) Representative images (montages) of BLOs generated from lung tip epithelium isolated at E9.5 (11 days in culture), E10.5 (11 days), E11.5 (11 days), E12.0 (8 days), E12.5 (8 days), E13.0 (11 days), E14.0 (13 days), and E10.5 (11 days) from C57 mice. Scale bars, 500 μm.

(B) Representative images of organoids generated from lung distal epithelial cluster isolated at E15.0, E16.0, E17.0, and E18.0. Scale bars, 500 μm.

(C) Percentage of organoids displaying branching structures across embryonic stages from E9.5 to E14.0. More than 10 organoids were quantified per developmental stage. The exact number of organoids analyzed in each experimental batch is listed in Table S3. Each dot represents an independent experimental batch. Error bars indicate mean ± SD.

(D) Violin plots showing the number of detected genes (left) and the percentage of mitochondrial transcripts (right) in BLOs across all indicated groups.

(E) UMAP visualization of BLOs at comparable differentiation stages (E10.5 and E11.5 at day 11; E12.5 at day 9).

(F) Dot plot summarizing marker gene expression across identified BLO cell types.

(G) Cellular composition of BLOs.

(H) Representative images (montages) of E11.0-derived BLOs cultured for 18, 30, and 60 days. Scale bars, 500 μm.

(I) Quantification of organoid width and height for E11.0- and E13.0-derived BLOs after 30 days in culture (n = 3). Dots represent individual BLOs. Error bars indicate mean ± SD.

See also Figure S5.

Together, these results define a restricted developmental window from E9.5 to E14.0 during which lung progenitor cells retain intrinsic competence for *in vitro* branching morphogenesis.

Comparable features of BLOs derived from E9.5 to E14.0 lung tip epithelium

To compare the cellular composition of BLOs derived from different genetic backgrounds and developmental stages, we performed scRNA-seq on day 11 BLOs generated from lung bud tip epithelium of distinct origins. High-quality scRNA-seq datasets were obtained for all samples (Figure 6D). UMAP analysis revealed that BLOs derived from E10.5 embryos of both ICR and C57BL/6 backgrounds, as well as those derived from E11.5 and E12.5 ICR embryos, clustered closely and largely overlapped (Figure 6E), indicating similar cellular states across conditions.

Cell-type annotation showed that all BLOs contained comparable epithelial compositions, encompassing both distal and proximal lung epithelial lineages (Figures 6E and 6F). Consistent with our earlier observations, distal epithelial populations constituted the predominant cell type in BLOs, whereas proximal airway epithelial cells represented only a minor fraction (Figure 6G). Although the relative proportions of individual cell types varied modestly among BLOs, the overall cellular composition was largely conserved. Neuroendocrine epithelial cells were not detected in BLOs derived from E10.5 C57BL/6 or E11.5 ICR embryos, which likely reflects their low abundance and limited capture efficiency in these samples.

To further evaluate molecular similarities and differentiation trajectories, we collected BLOs derived from E9.5 to E14.0 lung bud tip epithelium at multiple time points for bulk RNA-seq. Transcriptomic analyses revealed that all BLO samples clustered tightly and exhibited high pairwise correlations, yet they were clearly separated from their corresponding primary tip epithelium (Figure S5B), indicating transcriptional remodeling during *in vitro* culture. PCA showed that BLO transcriptomes were ordered primarily by culture duration rather than developmental origin (Figure S5C), suggesting a shared differentiation trajectory over time.

Consistent with this progression, extended culture resulted in downregulation of stem cell associated genes, whereas upregulated genes were enriched for pathways related to lung epithelial differentiation, including alveolar maturation and lipid metabolic processes (Figures S5D and S5E). Notably, BLOs derived from different developmental stages could be maintained long term in culture. Over the course of 1 month, BLOs underwent substantial expansion, reaching diameters of approximately 1 cm and occupying the surrounding Matrigel matrix (Figures 6H and 6I).

Despite these shared features, we observed subtle differences in growth dynamics. BLOs derived from E13.0 lung tip epithelium underwent proximodistal patterning during branching morphogenesis between days 2 and 8 of culture, similar to E10.5 BLOs (Figure S5F). However, E13.0-derived BLOs initiated branching, and expression of alveolar markers SFTPC and HOPX was activated earlier than in E10.5-derived BLOs (Figures S5A and S5G). These findings indicate that BLOs derived from E9.5 to E14.0 embryos share comparable transcriptional landscapes and differentiation programs, while retaining stage-dependent differences in the timing of branching and lineage maturation.

Transplantation of BLO-derived cells ameliorates bleomycin-induced pulmonary fibrosis

To evaluate the functional potential of BLO-derived cells *in vivo*, we tested their regenerative efficacy in a bleomycin-induced pulmonary fibrosis model. Pulmonary fibrosis is a chronic and progressive disease characterized by extensive destruction of the distal lung epithelium,[35] for which effective regenerative strategies remain limited. Given the robust capacity of BLOs to generate distal lung epithelial lineages, we hypothesized that transplantation of BLO-derived cells could promote epithelial regeneration and attenuate fibrotic pathology.

BLOs were generated from E10.5 lung bud tip epithelium constitutively expressing mtdTomato and cultured for 11 days (Figures S6A and S6B). At this stage, BLOs exhibited cellular features resembling those of the E15.5–E16.0 fetal lung (Figure S2D). Previous studies have reported that E15.5 whole lung cells exhibit the highest engraftment efficiency following transplantation compared with other developmental stages.[36] However, transplantation of E15.5 whole lung cells cannot reconstruct alveolar structures *in vivo*. Whether transplantation of E15.5 epithelium alone can regenerate injured lung tissue remains unclear. To test it, BLOs were subsequently dissociated into single-cell suspensions and delivered via intratracheal instillation into mice subjected to bleomycin-induced lung injury. Engraftment and regenerative outcomes were assessed at 7, 21, 56, and 180 days post-transplantation (dpt) (Figure S6A). At 7 dpt, mtdTomato$^+$ donor-derived cells were detected within injured lung regions, indicating successful survival and engraftment. Notably, the mtdTomato$^+$ cell population expanded at 21, 56, and 180 dpt (Figures 7A and S6D), demonstrating long-term persistence, proliferation, and integration of BLO-derived cells *in vivo*.

To assess the impact of transplantation on fibrotic pathology, we performed micro-computed tomography (micro-CT) analysis, which revealed a marked reduction in fibrotic lesions in transplanted mice compared with bleomycin-only controls (Figure 7B). Histological analyses using hematoxylin and eosin (H&E) and Masson's trichrome staining further demonstrated substantial restoration of lung parenchymal architecture and a pronounced decrease in collagen deposition following BLO-derived cell transplantation (Figures 7C and S6C).

Immunofluorescence staining using specific markers for alveolar epithelium, endothelial cells, and mesenchymal cells confirmed that engrafted tdTomato$^+$ BLO-derived cells integrated with host endothelial and mesenchymal compartments, consistent with their participation in the reconstitution of gas-exchange units (Figures 7D and 7E). Consistently, pulmonary function tests (PFTs) revealed significant functional improvements in transplanted mice, including increased total lung capacity and forced vital capacity, reduced airway resistance, and enhanced lung compliance, relative to bleomycin-treated controls (Figure 7F).

To assess whether BLO-derived cells from different stages exhibit similar regenerative capacity, we additionally transplanted cells derived from day 18 BLOs generated from E10.5 tissue and day 10 BLOs generated from E12.5 tissue. In all cases, donor-derived cells engrafted and formed new alveolar structures within injured lung regions (Figures S6E–S6H), indicating that regenerative potential is maintained across these BLO stages.

To precisely define the *in vivo* differentiation states of BLO-derived cells during lung repair, we performed scRNA-seq

CellPress
OPEN ACCESS

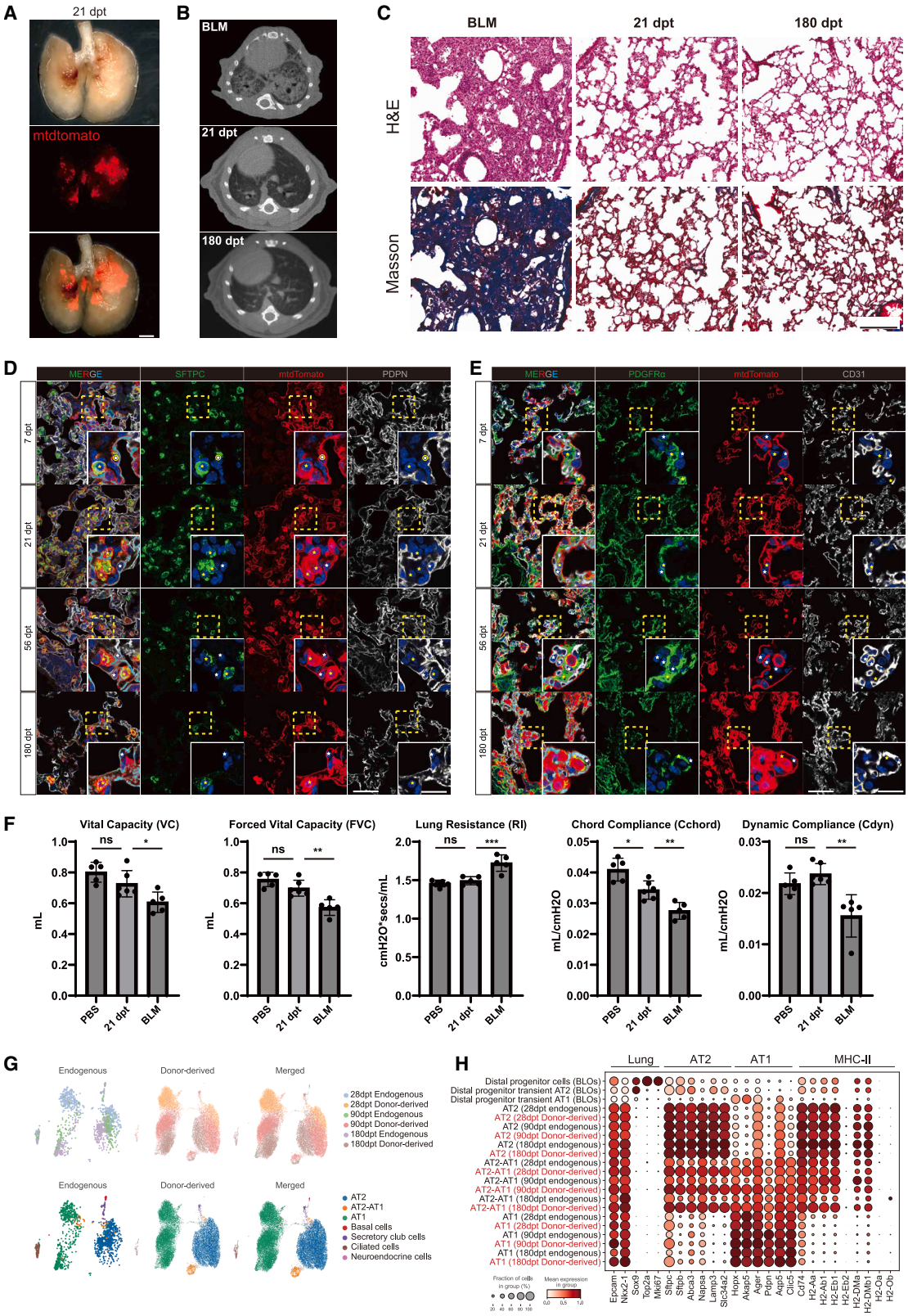

Figure 7. Transplantation of BLO-derived cells ameliorates BLM-induced pulmonary fibrosis

(A) Direct fluorescence stereomicroscopy image showing mtdTomato$^+$ BLO-derived cells engrafted in lungs at 21 dpt. Scale bar, 2 mm.

(B) Representative CT images of lungs from the bleomycin (BLM)-injured control group and the mtdTomato$^+$ BLO cell transplantation group at 21 and 180 dpt.

(legend continued on next page)

on sorted mtdTomato$^+$(donor-derived) and mtdTomato$^-$(endogenous) cell populations at 28 and 90 dpt (Figures S7A and S7B). Cell-type annotation based on lineage-specific markers revealed that the mtdTomato$^+$ population was predominantly composed of epithelial cells (Figures S7C–S7F). Among these, AT1 cells represented the largest fraction (50%–64.8%), followed by AT2 cells (32.5%–44.8%) and a small population of AT2-to-AT1 transitional cells (2.2%–3.3%) (Figures 7G and S7G). Importantly, donor-derived alveolar epithelial cells uniformly lacked expression of Sox9 and instead expressed high levels of mature lineage markers. AT1 cells expressed *Pdpn*, *Clic5*, and *Ager*, whereas AT2 cells expressed *Abca3*, *Lamp3*, and *Slc34a2* (Figure 7H). These results indicate that day 11 BLO-derived cells undergo further differentiation and maturation *in vivo* following transplantation, contributing to epithelial repair of the injured lung. Notably, BLO-derived AT1 and AT2 cells exhibited high expression of MHC-class-II-associated genes involved in antigen presentation and host defense,[37] with expression levels comparable to those observed in endogenous alveolar epithelial cells (Figure 7H). This suggests that BLO-derived alveolar cells acquire functional properties resembling their native counterparts. In contrast, scRNA-seq revealed minimal contributions from proximal airway epithelial lineages, including basal, secretory, and ciliated cells (Figure S7H), consistent with the distal fate bias observed during *in vitro* BLO differentiation. These findings were further validated by *in situ* immunofluorescence analysis (Figure S7I).

DISCUSSION

In summary, BLOs recapitulate key features of lung epithelial development, including canonical branching morphogenesis, proximodistal patterning, epithelial lineage progression, and alveolar maturation (Table S4), providing a robust and versatile platform for investigating lung development and regeneration.

Branching morphogenesis is a fundamental process underlying lung development, coordinating epithelial growth, proximodistal patterning, and functional maturation.[18,19,22] To date, *in vitro* studies of this process have largely relied on two experimental platforms: whole lung explant cultures and lung organoid systems. Whole lung explants preserve native tissue architecture and cellular diversity but can typically be maintained for only 2–3 days,[38,39] limiting experimental perturbation and long-term analysis. Moreover, the simultaneous presence of proximal and distal epithelium, together with mesenchymal and endothelial compartments, complicates the dissection of epithelial-intrinsic mechanisms governing proximodistal and lineage differentiation. In contrast, BLOs are initiated exclusively from lung bud tip epithelium and are devoid of mesenchymal components and pre-existing proximal epithelium. Despite this minimal starting configuration, BLOs undergo robust branching morphogenesis, proximodistal patterning, and epithelial lineage differentiation in a manner reminiscent of *in vivo* lung development. Notably, BLOs grow rapidly, reaching diameters approaching 1 cm within 1 month, and maintain stable multilevel branching architectures over 60 days. This extended temporal window enables systematic perturbation and longitudinal analysis of branching morphogenesis and epithelial differentiation, which is difficult to achieve with whole lung explant culture models. On the other hand, BLOs derived from PSCs have been reported previously[12]; however, these systems often exhibit disorganized branching patterns, aberrant spatial distribution of cell types, and limited maturation of alveolar lineages, particularly the absence of fully differentiated AT1 cells *in vitro*. In contrast, BLOs display region-specific cellular organization and generate alveolar-sac-like structures composed of mature AT1 cells with characteristic flattened morphology. Moreover, BLOs recapitulate stereotyped branching programs—domain branching, planar bifurcation, and orthogonal bifurcation—that closely mirror those observed during native lung development, underscoring their fidelity as a developmental model.

Multiple factors have been implicated in regulating lung branching morphogenesis.[19,22] *In vivo* studies have emphasized the essential roles of mesenchymal cells, particularly smooth muscle progenitors, in shaping epithelial branching.[40] Surprisingly, BLOs undergo extensive and stereotypic branching morphogenesis in the absence of mesenchymal components. Furthermore, fragmentation of the initiating lung bud tip epithelium does not impair branching capacity, indicating that neither epithelial-mesenchymal physical interactions nor the initial spatial integrity of the epithelium is strictly required for branching. Instead, our findings support the notion that soluble niche signals—classically provided by mesenchyme *in vivo*—are sufficient to drive epithelial branching programs.[22] Consistent with this paradigm, BLO formation and growth are dependent on Wnt and FGF signaling. Removal of the Wnt agonist CHIR99021 or FGF7 completely abolished BLO growth and branching. Interestingly, withdrawal of FGF10 had minimal effects on branching, suggesting ligand-specific roles within the FGF family. This observation aligns with previous studies identifying FGF7, but not FGF10, as essential for the growth

(C) H&E and Masson's trichrome staining of lung sections under conditions shown in (B). Scale bar, 200 μm.
(D) Immunofluorescence analysis of lung sections at 7, 21, 56, and 180 dpt showing mtdTomato$^+$ BLO-derived cells co-expressing SFTPC or PDPN. Yellow stars indicate cells co-expressing mtdTomato and SFTPC, and white stars indicate cells co-expressing mtdTomato and PDPN. Insets show higher-magnification views of regions outlined by yellow dashed boxes. Nuclei were counterstained with DAPI. Scale bars, 50 (main) and 20 μm (insets).
(E) Immunofluorescence staining of lung sections at 7, 21, 56, and 180 dpt illustrating the spatial relationship between engrafted mtdTomato$^+$ donor cells and host stromal and endothelial compartments. Co-staining for PDGFRα and CD31. Yellow stars denote PDGFRα$^+$ mesenchymal cells adjacent to donor cells, and white stars denote CD31$^+$ endothelial cells adjacent to donor cells. Insets show higher-magnification views of boxed regions. Scale bars, 50 (main) and 20 μm (insets).
(F) Pulmonary function test parameters measured in PBS sham-operated controls ($n = 5$), BLM-injured controls ($n = 5$), and BLM-injured mice transplanted with mtdTomato$^+$ BLO-derived cells ($n = 6$). Error bars represent mean ± SEM. Statistical significance was assessed by one-way ANOVA with multiple comparisons. $^*p < 0.05$, $^{**}p < 0.01$, $^{***}p < 0.001$.
(G) UMAP visualization of endogenous (1,423 cells; mtdTomato-negative) and donor-derived (22,248 cells; mtdTomato-positive) epithelial populations at 28, 90, and 180 dpt, colored by annotated cell types. Cells are fluorescence-activated cell sorting (FACS) sorted on tdTomado, and only epithelial cells are plotted.
(H) Dot plot comparing the expression of lung lineage markers between endogenous epithelial cells and BLO-derived donor cells.
See also Figures S6 and S7.

and self-renewal of lung-bud-tip-derived epithelial stem cells.[41] Beyond Wnt and FGF signaling, Vc and MTG also contributed to BLO branching morphogenesis and lineage maturation. Our previous work demonstrated that Vc markedly promoted PSCs generation, primarily through epigenetic mechanisms involving histone modifications[33] and DNA methylation.[34] Interestingly, in BLOs, Vc uniquely suppressed chromatin remodeling and cell-cycle-associated genes that are highly expressed in distal epithelial progenitors, thereby facilitating AT1 and AT2 cell maturation. These effects were distinct from those of MTG and FGF10, suggesting that Vc promotes epithelial maturation through specific epigenetic transitions, the precise mechanisms of which warrant further investigation.

In addition to extrinsic cues, the intrinsic competence of the epithelial starting population critically determines BLO formation. We found that lung bud tip epithelium isolated between E9.5 and E14.0 could generate BLOs, whereas tip or distal epithelial tissues from E14.5 to E18.0 formed only simple spherical organoids. Branching efficiency declined progressively after E12.0, highlighting a restricted developmental window during which epithelial progenitors retain intrinsic branching capacity. Although BLOs derived from E9.5 to E14.0 embryos exhibited comparable cellular and molecular features, they displayed subtle differences in growth and differentiation dynamics, indicating that developmental history influences the timing—but not the overall trajectory—of *in vitro* differentiation. These findings further suggest that, beyond medium composition, the induction of lung epithelial progenitors equivalent to their *in vivo* counterparts is a critical consideration for optimizing PSC-derived lung organoid systems.

BLOs comprise heterogeneous populations of distal and proximal lung epithelial cells whose composition dynamically evolves over prolonged culture. During early stages (days 1–11), $SOX2^+$ proximal progenitors localize centrally, whereas $Sox9^+$ distal progenitors occupy branching tips. $ICAM1^+$ transitional cells are detected at the interface between these domains, indicating a spatially defined intermediate state. scRNA-seq further confirms the presence of distal progenitors, immature alveolar cells, and SOX2+ proximal airway progenitors, as well as differentiated proximal cell types, including neuroendocrine, ciliated, and secretory club cells. At later stages, the progenitor pool contracts, mature AT2 cells become predominant, and mature AT1 cells and transitional states emerge along the alveolar differentiation continuum. This temporal progression reflects both the intrinsic multipotency of lung bud tip epithelial cells and sustained activation of Wnt signaling via CHIR99021. Consistent with previous reports showing that Wnt activation promotes distal fate specification while suppressing proximal differentiation,[42] prolonged Wnt signaling in BLOs drives progressive maturation toward distal alveolar lineages. Consequently, proximal epithelial differentiation is relatively restrained. Modulating or counterbalancing Wnt activity may therefore be required to generate organoids encompassing the full spectrum of lung epithelial lineages. Importantly, BLOs not only generate large numbers of mature AT1 and AT2 cells but also reconstruct distal lung architecture, forming micro-alveolar sac structures. These features position BLOs as a powerful platform for establishing complex alveolar structures involving epithelial-immune-endothelial interactions and investigating their cellular crosstalk that are central to lung physiology and disease.

Finally, the chemically defined nature of the BLO induction system provides a clean and tractable experimental framework for mechanistic studies. Recent large-scale single-cell atlases have greatly expanded our understanding of lung development,[43–50] revealing numerous candidate regulators of epithelial fate specification and branching morphogenesis. However, functional validation of these factors *in vivo* remains challenging due to system complexity and the time required to generate genetic models. BLOs offer an efficient alternative for testing genetic and epigenetic regulators identified through atlas studies, enabling rapid dissection of their roles in branching morphogenesis and lineage differentiation in epithelial-specific contexts. Notably, although BLO formation occurs independently of mesenchymal support *in vitro*, BLO-derived cells retain the capacity to integrate with host stromal and endothelial cells *in vivo*, contribute to alveolar reconstruction, and improve lung function. These findings suggest potential utility of BLO-derived cells in lung regenerative applications.

Limitations of the study

Despite its utility, the current BLO system has several limitations. BLOs are derived from embryonic mouse lung tissue, limiting scalability and direct translation to human systems. In addition, BLOs generate a minor fraction of proximal airway lineages under current culture conditions. Future studies should focus on deriving BLOs from PSCs or expandable progenitors and optimizing signaling conditions to more fully recapitulate lung epithelial diversity and development.

RESOURCE AVAILABILITY

Lead contact

Requests for further information and resources should be directed to and will be fulfilled by the lead contact, Shangtao Cao (cao_shangtao@gzlab.ac.cn).

Materials availability

This study did not generate new unique reagents.

Data and code availability

- All sequencing data have been deposited at GEO as GSE303739 and are publicly available as of the date of publication. This paper analyzes existing, publicly available data, accessible at GSA: CRA003171[28]; GEO: GSE165063[46]; GEO: GSE149563[47]; GEO: GSE141259[48]; GEO: GSE124872.[49]
- All original code has been deposited at Zenodo and is publicly available at 10.5281/zenodo.20307885 as of the date of publication.
- Any additional information required to reanalyze the data reported in this paper is available from the lead contact upon request.

ACKNOWLEDGMENTS

This research was supported by grants from Major Project of Guangzhou National Laboratory (GZNL2023A02005, GZNL2024A02005, and GZNL 2025C02029), National Key R&D Program of China (2024YFA1802300 and 2025YFA1804200), National Natural Science Foundation of China (32300665, 82470704 and 92068201), Science and Technology Planning Project of Guangdong Province, China (2023TQ07A630), and Pearl River Talent Recruitment Program (2021ZT09Y233). We also thank a lot for public

instrument service center Guangzhou National Laboratory and Guangzhou Branch of the Supercomputing Center of the Chinese Academy of Sciences.

AUTHOR CONTRIBUTIONS

S. Cao initiated the project. S. Cao, M.P., B.C., M.M., and M.Z. designed the experiments. M.P., B.C., and C.D. performed lung organoid experiments. M.P., G.L., Y. Chen, S. Chen, X.Q., D.T., and Y.T. performed animal model and cell transplantation experiments. B.C., Z.F., Y. Cheng, and C.Z. prepared RNA-seq and scRNA-seq libraries construction. R.Z. and H.C. preformed bioinformatics and single cell data analysis. A.G., C.D., J.H., and Y.H. recorded BLOs dynamics. Y.D., Y.F., S.L., W.H., and S.Y. performed BLOs molecular validation. D.Q. and Y.L. provided help for the project. S. Cao, M.M., M.Z., J.C., M.P., B.C., A.G., R.Z., and H.C. wrote the manuscript. S. Cao, M.M., M.Z., J.C., and D.P. supervised the whole study and approved the final version.

DECLARATION OF INTERESTS

S. Cao, M.P., B.C., M.M., and M.Z. have a patent application related to this work.

DECLARATION OF GENERATIVE AI AND AI-ASSISTED TECHNOLOGIES IN THE WRITING PROCESS

During manuscript preparation, we used ChatGPT to improve language clarity and readability. All content was carefully reviewed and edited by the authors, who take full responsibility for the final manuscript.

STAR★METHODS

Detailed methods are provided in the online version of this paper and include the following:

- KEY RESOURCES TABLE
- EXPERIMENTAL MODEL AND STUDY PARTICIPANT DETAILS
  - Animals
  - Organoid culture
- METHOD DETAILS
  - Isolation and microdissection of mouse embryonic lung distal tip epithelium for BLO induction
  - Culture medium formulation for BLO induction
  - Assessment of branching-inducing capacity of lung tip epithelium
  - Live-cell imaging
  - BLOs skeletonization analysis
  - Branching tree similarity analysis
  - Bleomycin-induced lung injury model and cell transplantation
  - Measurement of mouse lung function
  - Small-animal micro-computed tomography (micro-CT)
  - Bulk RNA library preparation and sequencing
  - Single-cell RNA library preparation and sequencing
  - Flow cytometric sorting and scRNA-seq of post-transplant lung tissues
  - Bulk RNA-seq data analysis
  - Single-cell RNA-seq analysis of BLOs
  - Integrated analysis of multiple datasets
  - ScRNA-seq analysis of post-transplant lung tissue
  - Histopathological analysis
  - Immunostaining
  - Whole-mount immunostaining and live-cell staining
- QUANTIFICATION AND STATISTICAL ANALYSES
  - Statistical analysis
  - Software

SUPPLEMENTAL INFORMATION

Supplemental information can be found online at https://doi.org/10.1016/j.devcel.2026.05.012.

Received: July 1, 2025
Revised: January 30, 2026
Accepted: May 22, 2026
Published: June 18, 2026

REFERENCES

1. Clevers, H. (2016). Modeling Development and Disease with Organoids. Cell *165*, 1586–1597. https://doi.org/10.1016/j.cell.2016.05.082.
2. Kretzschmar, K., and Clevers, H. (2016). Organoids: Modeling Development and the Stem Cell Niche in a Dish. Dev. Cell *38*, 590–600. https://doi.org/10.1016/j.devcel.2016.08.014.
3. Gotoh, S., Ito, I., Nagasaki, T., Yamamoto, Y., Konishi, S., Korogi, Y., Matsumoto, H., Muro, S., Hirai, T., Funato, M., et al. (2014). Generation of alveolar epithelial spheroids via isolated progenitor cells from human pluripotent stem cells. Stem Cell Rep. *3*, 394–403. https://doi.org/10.1016/j.stemcr.2014.07.005.
4. Dye, B.R., Hill, D.R., Ferguson, M.A.H., Tsai, Y.H., Nagy, M.S., Dyal, R., Wells, J.M., Mayhew, C.N., Nattiv, R., Klein, O.D., et al. (2015). In vitro generation of human pluripotent stem cell derived lung organoids. eLife *4*, e05098. https://doi.org/10.7554/eLife.05098.
5. Barkauskas, C.E., Chung, M.I., Fioret, B., Gao, X., Katsura, H., and Hogan, B.L.M. (2017). Lung organoids: current uses and future promise. Development *144*, 986–997. https://doi.org/10.1242/dev.140103.
6. Nikolić, M.Z., Caritg, O., Jeng, Q., Johnson, J.A., Sun, D., Howell, K.J., Brady, J.L., Laresgoiti, U., Allen, G., Butler, R., et al. (2017). Human embryonic lung epithelial tips are multipotent progenitors that can be expanded in vitro as long-term self-renewing organoids. eLife *6*, e26575. https://doi.org/10.7554/eLife.26575.
7. Yamamoto, Y., Gotoh, S., Korogi, Y., Seki, M., Konishi, S., Ikeo, S., Sone, N., Nagasaki, T., Matsumoto, H., Muro, S., et al. (2017). Long-term expansion of alveolar stem cells derived from human iPS cells in organoids. Nat. Methods *14*, 1097–1106. https://doi.org/10.1038/nmeth.4448.
8. Nichane, M., Javed, A., Sivakamasundari, V., Ganesan, M., Ang, L.T., Kraus, P., Lufkin, T., Loh, K.M., and Lim, B. (2017). Isolation and 3D expansion of multipotent Sox9+ mouse lung progenitors. Nat. Methods *14*, 1205–1212. https://doi.org/10.1038/nmeth.4498.
9. Jacob, A., Morley, M., Hawkins, F., McCauley, K.B., Jean, J.C., Heins, H., Na, C.L., Weaver, T.E., Vedaie, M., Hurley, K., et al. (2017). Differentiation of Human Pluripotent Stem Cells into Functional Lung Alveolar Epithelial Cells. Cell Stem Cell *21*, 472–488.e10. https://doi.org/10.1016/j.stem.2017.08.014.
10. Miller, A.J., Yu, Q., Czerwinski, M., Tsai, Y.H., Conway, R.F., Wu, A., Holloway, E.M., Walker, T., Glass, I.A., Treutlein, B., et al. (2020). In Vitro and In Vivo Development of the Human Airway at Single-Cell Resolution. Dev. Cell *53*, 117–128.e6. https://doi.org/10.1016/j.devcel.2020.01.033.
11. Lim, K., Donovan, A.P.A., Tang, W., Sun, D., He, P., Pett, J.P., Teichmann, S.A., Marioni, J.C., Meyer, K.B., Brand, A.H., et al. (2023). Organoid modeling of human fetal lung alveolar development reveals mechanisms of cell fate patterning and neonatal respiratory disease. Cell Stem Cell *30*, 20–37.e9. https://doi.org/10.1016/j.stem.2022.11.013.
12. Chen, Y.W., Huang, S.X., de Carvalho, A.L.R.T., Ho, S.H., Islam, M.N., Volpi, S., Notarangelo, L.D., Ciancanelli, M., Casanova, J.L., Bhattacharya, J., et al. (2017). A three-dimensional model of human lung development and disease from pluripotent stem cells. Nat. Cell Biol. *19*, 542–549. https://doi.org/10.1038/ncb3510.
13. Mithal, A., Capilla, A., Heinze, D., Berical, A., Villacorta-Martin, C., Vedaie, M., Jacob, A., Abo, K., Szymaniak, A., Peasley, M., et al. (2020). Generation of mesenchyme free intestinal organoids from human induced pluripotent stem cells. Nat. Commun. *11*, 215. https://doi.org/10.1038/s41467-019-13916-6.
14. Kagawa, H., Javali, A., Khoei, H.H., Sommer, T.M., Sestini, G., Novatchkova, M., Scholte op Reimer, Y., Castel, G., Bruneau, A., Maenhoudt, N., et al. (2022). Human blastoids model blastocyst

development and implantation. Nature *601*, 600–605. https://doi.org/10.1038/s41586-021-04267-8.

15. Tarazi, S., Aguilera-Castrejon, A., Joubran, C., Ghanem, N., Ashouokhi, S., Roncato, F., Wildschutz, E., Haddad, M., Oldak, B., Gomez-Cesar, E., et al. (2022). Post-gastrulation synthetic embryos generated ex utero from mouse naive ESCs. Cell *185*, 3290–3306.e25. https://doi.org/10.1016/j.cell.2022.07.028.
16. Karvas, R.M., Zemke, J.E., Ali, S.S., Upton, E., Sane, E., Fischer, L.A., Dong, C., Park, K.M., Wang, F., Park, K., et al. (2023). 3D-cultured blastoids model human embryogenesis from pre-implantation to early gastrulation stages. Cell Stem Cell *30*, 1148–1165.e7. https://doi.org/10.1016/j.stem.2023.08.005.
17. Li, H., Guan, W., Huang, J., Shen, P., Wu, J., Luo, H., Yang, Y., Ning, S., Chang, L., Zhao, H., et al. (2025). A complete model of mouse embryogenesis through organogenesis enabled by chemically induced embryo founder cells. Cell *188*, 5912–5930.e20. https://doi.org/10.1016/j.cell.2025.07.018.
18. Metzger, R.J., Klein, O.D., Martin, G.R., and Krasnow, M.A. (2008). The branching programme of mouse lung development. Nature *453*, 745–750. https://doi.org/10.1038/nature07005.
19. Goodwin, K., and Nelson, C.M. (2020). Branching morphogenesis. Development *147*, dev184499. https://doi.org/10.1242/dev.184499.
20. Swarr, D.T., and Morrisey, E.E. (2015). Lung endoderm morphogenesis: gasping for form and function. Annu. Rev. Cell Dev. Biol. *31*, 553–573. https://doi.org/10.1146/annurev-cellbio-100814-125249.
21. Nikolić, M.Z., Sun, D., and Rawlins, E.L. (2018). Human lung development: recent progress and new challenges. Development *145*, dev163485. https://doi.org/10.1242/dev.163485.
22. Varner, V.D., and Nelson, C.M. (2014). Cellular and physical mechanisms of branching morphogenesis. Development *141*, 2750–2759. https://doi.org/10.1242/dev.104794.
23. Basil, M.C., Katzen, J., Engler, A.E., Guo, M., Herriges, M.J., Kathiriya, J.J., Windmueller, R., Ysasi, A.B., Zacharias, W.J., Chapman, H.A., et al. (2020). The Cellular and Physiological Basis for Lung Repair and Regeneration: Past, Present, and Future. Cell Stem Cell *26*, 482–502. https://doi.org/10.1016/j.stem.2020.03.009.
24. Chao, C.M., Yahya, F., Moiseenko, A., Tiozzo, C., Shrestha, A., Ahmadvand, N., El Agha, E., Quantius, J., Dilai, S., Kheirollahi, V., et al. (2017). Fgf10 deficiency is causative for lethality in a mouse model of bronchopulmonary dysplasia. J. Pathol. *241*, 91–103. https://doi.org/10.1002/path.4834.
25. Jones, M.R., Chong, L., and Bellusci, S. (2020). Fgf10/Fgfr2b Signaling Orchestrates the Symphony of Molecular, Cellular, and Physical Processes Required for Harmonious Airway Branching Morphogenesis. Front. Cell Dev. Biol. *8*, 620667. https://doi.org/10.3389/fcell.2020.620667.
26. Schuger, L., Varani, J., Mitra, R., Jr., and Gilbride, K. (1993). Retinoic acid stimulates mouse lung development by a mechanism involving epithelial-mesenchymal interaction and regulation of epidermal growth factor receptors. Dev. Biol. *159*, 462–473. https://doi.org/10.1006/dbio.1993.1256.
27. Ke, X., van Soldt, B., Vlahos, L., Zhou, Y., Qian, J., Laise, P., George, J., Capdevila, C., Glass, I., Yan, K., et al. (2025). Morphogenesis and regeneration share a conserved core transition cell state program that controls lung epithelial cell fate. Dev. Cell *60*, 819–836.e7. https://doi.org/10.1016/j.devcel.2024.11.017.
28. Cao, S., Lin, L., Feng, H., Chen, P., Wu, G., Cai, B., Pan, M., Shen, Q., Chen, H., Zhai, X., et al. (2026). Developmental chronology of mouse embryo from 2-cell stage through birth. Nat Cell Biol. https://doi.org/10.1038/s41556-026-01971-3.
29. Takahashi, Y., Izumi, Y., Kohno, M., Kawamura, M., Ikeda, E., and Nomori, H. (2011). Airway administration of dexamethasone, 3′-5′-cyclic adenosine monophosphate, and isobutylmethylxanthine facilitates compensatory lung growth in adult mice. Am. J. Physiol., Lung Cell. Mol. Physiol. *300*, L453–L461. https://doi.org/10.1152/ajplung.00100.2010.
30. Guo, M., Morley, M.P., Jiang, C., Wu, Y., Li, G., Du, Y., Zhao, S., Wagner, A., Cakar, A.C., Kouril, M., et al. (2023). Guided construction of single cell reference for human and mouse lung. Nat Commun *14*, 4566. https://doi.org/10.1038/s41467-023-40173-5.
31. Benlhabib, H., and Mendelson, C.R. (2011). Epigenetic regulation of surfactant protein A gene (SP-A) expression in fetal lung reveals a critical role for Suv39h methyltransferases during development and hypoxia. Mol. Cell. Biol. *31*, 1949–1958. https://doi.org/10.1128/MCB.01063-10.
32. Liberti, D.C., Zepp, J.A., Bartoni, C.A., Liberti, K.H., Zhou, S., Lu, M., Morley, M.P., and Morrisey, E.E. (2019). Dnmt1 is required for proximal-distal patterning of the lung endoderm and for restraining alveolar type 2 cell fate. Dev. Biol. *454*, 108–117. https://doi.org/10.1016/j.ydbio.2019.06.019.
33. Wang, T., Chen, K., Zeng, X., Yang, J., Wu, Y., Shi, X., Qin, B., Zeng, L., Esteban, M.A., Pan, G., et al. (2011). The histone demethylases Jhdm1a/1b enhance somatic cell reprogramming in a vitamin-C-dependent manner. Cell Stem Cell *9*, 575–587. https://doi.org/10.1016/j.stem.2011.10.005.
34. Chen, J., Guo, L., Zhang, L., Wu, H., Yang, J., Liu, H., Wang, X., Hu, X., Gu, T., Zhou, Z., et al. (2013). Vitamin C modulates TET1 function during somatic cell reprogramming. Nat. Genet. *45*, 1504–1509. https://doi.org/10.1038/ng.2807.
35. Lederer, D.J., and Martinez, F.J. (2018). Idiopathic Pulmonary Fibrosis. N. Engl. J. Med. *378*, 1811–1823. https://doi.org/10.1056/NEJMra1705751.
36. Shiraishi, K., Shichino, S., Tsukui, T., Hashimoto, S., Ueha, S., and Matsushima, K. (2019). Engraftment and proliferation potential of embryonic lung tissue cells in irradiated mice with emphysema. Sci. Rep. *9*, 3657. https://doi.org/10.1038/s41598-019-40237-x.
37. Shenoy, A.T., Lyon De Ana, C., Arafa, E.I., Salwig, I., Barker, K.A., Korkmaz, F.T., Ramanujan, A., Etesami, N.S., Soucy, A.M., Martin, I.M.C., et al. (2021). Antigen presentation by lung epithelial cells directs CD4+ TRM cell function and regulates barrier immunity. Nat. Commun. *12*, 5834. https://doi.org/10.1038/s41467-021-26045-w.
38. Del Moral, P.M., and Warburton, D. (2010). Explant culture of mouse embryonic whole lung, isolated epithelium, or mesenchyme under chemically defined conditions as a system to evaluate the molecular mechanism of branching morphogenesis and cellular differentiation. Methods Mol. Biol. *633*, 71–79. https://doi.org/10.1007/978-1-59745-019-5_5.
39. Yeganeh, B., Bilodeau, C., and Post, M. (2018). Explant Culture for Studying Lung Development. Methods Mol. Biol. *1752*, 81–90. https://doi.org/10.1007/978-1-4939-7714-7_8.
40. Kim, H.Y., Pang, M.F., Varner, V.D., Kojima, L., Miller, E., Radisky, D.C., and Nelson, C.M. (2015). Localized Smooth Muscle Differentiation Is Essential for Epithelial Bifurcation during Branching Morphogenesis of the Mammalian Lung. Dev. Cell *34*, 719–726. https://doi.org/10.1016/j.devcel.2015.08.012.
41. Miller, A.J., Hill, D.R., Nagy, M.S., Aoki, Y., Dye, B.R., Chin, A.M., Huang, S., Zhu, F., White, E.S., Lama, V., et al. (2018). In Vitro Induction and In Vivo Engraftment of Lung Bud Tip Progenitor Cells Derived from Human Pluripotent Stem Cells. Stem Cell Rep. *10*, 101–119. https://doi.org/10.1016/j.stemcr.2017.11.012.
42. McCauley, K.B., Hawkins, F., Serra, M., Thomas, D.C., Jacob, A., and Kotton, D.N. (2017). Efficient Derivation of Functional Human Airway Epithelium from Pluripotent Stem Cells via Temporal Regulation of Wnt Signaling. Cell Stem Cell *20*, 844–857.e6. https://doi.org/10.1016/j.stem.2017.03.001.
43. Cao, S., Feng, H., Yi, H., Pan, M., Lin, L., Zhang, Y.S., Feng, Z., Liang, W., Cai, B., Li, Q., et al. (2023). Single-cell RNA sequencing reveals the developmental program underlying proximal-distal patterning of the human lung at the embryonic stage. Cell Res. *33*, 421–433. https://doi.org/10.1038/s41422-023-00802-6.
44. He, P., Lim, K., Sun, D., Pett, J.P., Jeng, Q., Polanski, K., Dong, Z., Bolt, L., Richardson, L., Mamanova, L., et al. (2022). A human fetal lung cell atlas uncovers proximal-distal gradients of differentiation and key regulators of epithelial fates. Cell *185*, 4841–4860.e25. https://doi.org/10.1016/j.cell.2022.11.005.

45. Sountoulidis, A., Marco Salas, S., Braun, E., Avenel, C., Bergenstråhle, J., Theelke, J., Vicari, M., Czarnewski, P., Liontos, A., Abalo, X., et al. (2023). A topographic atlas defines developmental origins of cell heterogeneity in the human embryonic lung. Nat. Cell Biol. *25*, 351–365. https://doi.org/10.1038/s41556-022-01064-x.

46. Negretti, N.M., Plosa, E.J., Benjamin, J.T., Schuler, B.A., Habermann, A.C., Jetter, C.S., Gulleman, P., Bunn, C., Hackett, A.N., Ransom, M., et al. (2021). A single-cell atlas of mouse lung development. Development *148*, dev199512. https://doi.org/10.1242/dev.199512.

47. Zepp, J.A., Morley, M.P., Loebel, C., Kremp, M.M., Chaudhry, F.N., Basil, M.C., Leach, J.P., Liberti, D.C., Niethamer, T.K., Ying, Y., et al. (2021). Genomic, epigenomic, and biophysical cues controlling the emergence of the lung alveolus. Science *371*, eabc3172. https://doi.org/10.1126/science.abc3172.

48. Strunz, M., Simon, L.M., Ansari, M., Kathiriya, J.J., Angelidis, I., Mayr, C.H., Tsidiridis, G., Lange, M., Mattner, L.F., Yee, M., et al. (2020). Alveolar regeneration through a Krt8+ transitional stem cell state that persists in human lung fibrosis. Nat. Commun. *11*, 3559. https://doi.org/10.1038/s41467-020-17358-3.

49. Angelidis, I., Simon, L.M., Fernandez, I.E., Strunz, M., Mayr, C.H., Greiffo, F.R., Tsitsiridis, G., Ansari, M., Graf, E., Strom, T.M., et al. (2019). An atlas of the aging lung mapped by single cell transcriptomics and deep tissue proteomics. Nat. Commun. *10*, 963. https://doi.org/10.1038/s41467-019-08831-9.

50. Han, X., Zhou, Z., Fei, L., Sun, H., Wang, R., Chen, Y., Chen, H., Wang, J., Tang, H., Ge, W., et al. (2020). Construction of a human cell landscape at single-cell level. Nature *581*, 303–309. https://doi.org/10.1038/s41586-020-2157-4.

51. Schindelin, J., Arganda-Carreras, I., Frise, E., Kaynig, V., Longair, M., Pietzsch, T., Preibisch, S., Rueden, C., Saalfeld, S., Schmid, B., et al. (2012). Fiji: an open-source platform for biological-image analysis. Nat. Methods *9*, 676–682. https://doi.org/10.1038/nmeth.2019.

52. Hagberg, A., and Conway, D. (2020). Networkx: Network Analysis with Python. https://networkx.github.io.1031.

53. McInnes, L., Healy, J., and Melville, J. (2018). Umap: Uniform Manifold Approximation and Projection for Dimension Reduction. Preprint at arXiv. https://doi.org/10.48550/arXiv.1802.03426.

54. Archit, A., Freckmann, L., Nair, S., Khalid, N., Hilt, P., Rajashekar, V., Freitag, M., Teuber, C., Spitzner, M., Tapia Contreras, C., et al. (2025). Segment Anything for Microscopy. Nat. Methods *22*, 579–591. https://doi.org/10.1038/s41592-024-02580-4.

55. Hunter, J.D. (2007). Matplotlib: A 2D graphics environment. Comput. Sci. Eng. *9*, 90–95. https://doi.org/10.1109/MCSE.2007.55. https://doi.

56. Bordeu, I., Chatzeli, L., and Simons, B.D. (2023). Inflationary theory of branching morphogenesis in the mouse salivary gland. Nat. Commun. *14*, 3422. https://doi.org/10.1038/s41467-023-39124-x.

57. Langmead, B., and Salzberg, S.L. (2012). Fast gapped-read alignment with Bowtie 2. Nat. Methods *9*, 357–359. https://doi.org/10.1038/nmeth.1923.

58. Li, B., and Dewey, C.N. (2011). RSEM: accurate transcript quantification from RNA-Seq data with or without a reference genome. BMC Bioinform. *12*, 323. https://doi.org/10.1186/1471-2105-12-323.

59. Love, M.I., Huber, W., and Anders, S. (2014). Moderated estimation of fold change and dispersion for RNA-seq data with DESeq2. Genome Biol. *15*, 550. https://doi.org/10.1186/s13059-014-0550-8.

60. Huber, W., Carey, V.J., Gentleman, R., Anders, S., Carlson, M., Carvalho, B.S., Bravo, H.C., Davis, S., Gatto, L., Girke, T., et al. (2015). Orchestrating high-throughput genomic analysis with Bioconductor. Nat. Methods *12*, 115–121. https://doi.org/10.1038/nmeth.3252.

61. Kumar, L., and E Futschik, M. (2007). Mfuzz: a software package for soft clustering of microarray data. Bioinformation *2*, 5–7. https://doi.org/10.6026/97320630002005.

62. Yu, G., Wang, L.G., Han, Y., and He, Q.Y. (2012). clusterProfiler: an R package for comparing biological themes among gene clusters. Omics *16*, 284–287. https://doi.org/10.1089/omi.2011.0118.

63. Wickham, H. (2016). Data Analysis. In ggplot2: Elegant Graphics for Data Analysis (Springer), pp. 189–201.

64. Dobin, A., Davis, C.A., Schlesinger, F., Drenkow, J., Zaleski, C., Jha, S., Batut, P., Chaisson, M., and Gingeras, T.R. (2013). STAR: ultrafast universal RNA-seq aligner. Bioinformatics *29*, 15–21. https://doi.org/10.1093/bioinformatics/bts635.

65. Wolf, F.A., Angerer, P., and Theis, F.J. (2018). SCANPY: large-scale single-cell gene expression data analysis. Genome Biol. *19*, 15. https://doi.org/10.1186/s13059-017-1382-0.

66. Wolock, S.L., Lopez, R., and Klein, A.M. (2019). Scrublet: computational identification of cell doublets in single-cell transcriptomic data. Cell Syst. *8*, 281–291.e9. https://doi.org/10.1016/j.cels.2018.11.005.

67. Lopez, R., Regier, J., Cole, M.B., Jordan, M.I., and Yosef, N. (2018). Deep generative modeling for single-cell transcriptomics. Nat. Methods *15*, 1053–1058. https://doi.org/10.1038/s41592-018-0229-2.

68. Xu, C., Lopez, R., Mehlman, E., Regier, J., Jordan, M.I., and Yosef, N. (2021). Probabilistic harmonization and annotation of single-cell transcriptomics data with deep generative models. Mol. Syst. Biol. *17*, e9620. https://doi.org/10.15252/msb.20209620.

69. Becht, E., McInnes, L., Healy, J., Dutertre, C.A., Kwok, I.W.H., Ng, L.G., Ginhoux, F., and Newell, E.W. (2018). Dimensionality reduction for visualizing single-cell data using UMAP. Nat. Biotechnol. https://doi.org/10.1038/nbt.4314.

70. Haghverdi, L., Buettner, F., and Theis, F.J. (2015). Diffusion maps for high-dimensional single-cell analysis of differentiation data. Bioinformatics *31*, 2989–2998. https://doi.org/10.1093/bioinformatics/btv325.

71. Setty, M., Kiseliovas, V., Levine, J., Gayoso, A., Mazutis, L., and Pe'er, D. (2019). Characterization of cell fate probabilities in single-cell data with Palantir. Nat. Biotechnol. *37*, 451–460. https://doi.org/10.1038/s41587-019-0068-4.

72. Lange, M., Bergen, V., Klein, M., Setty, M., Reuter, B., Bakhti, M., Lickert, H., Ansari, M., Schniering, J., Schiller, H.B., et al. (2022). CellRank for directed single-cell fate mapping. Nat. Methods *19*, 159–170. https://doi.org/10.1038/s41592-021-01346-6.

73. Korsunsky, I., Millard, N., Fan, J., Slowikowski, K., Zhang, F., Wei, K., Baglaenko, Y., Brenner, M., Loh, P.R., and Raychaudhuri, S. (2019). Fast, sensitive and accurate integration of single-cell data with Harmony. Nat. Methods *16*, 1289–1296. https://doi.org/10.1038/s41592-019-0619-0.

74. Hafemeister, C., and Satija, R. (2019). Normalization and variance stabilization of single-cell RNA-seq data using regularized negative binomial regression. Genome Biol. *20*, 296. https://doi.org/10.1186/s13059-019-1874-1.

75. Stuart, T., Butler, A., Hoffman, P., Hafemeister, C., Papalexi, E., Mauck, W.M., 3rd, Hao, Y., Stoeckius, M., Smibert, P., and Satija, R. (2019). Comprehensive Integration of Single-Cell Data. Cell *177*, 1888–1902.e21. https://doi.org/10.1016/j.cell.2019.05.031.

76. Feng, H., Lin, L., and Chen, J. (2022). scDIOR: single cell RNA-seq data IO software. BMC Bioinform. *23*, 16. https://doi.org/10.1186/s12859-021-04528-3.

77. Wolf, F.A., Hamey, F.K., Plass, M., Solana, J., Dahlin, J.S., Göttgens, B., Rajewsky, N., Simon, L., and Theis, F.J. (2019). PAGA: graph abstraction reconciles clustering with trajectory inference through a topology preserving map of single cells. Genome Biol. *20*, 59. https://doi.org/10.1186/s13059-019-1663-x.

78. Jacomy, M., Venturini, T., Heymann, S., and Bastian, M. (2014). ForceAtlas2, a continuous graph layout algorithm for handy network visualization designed for the Gephi software. PLoS One *9*, e98679. https://doi.org/10.1371/journal.pone.0098679.

79. Law, C.W., Chen, Y., Shi, W., and Smyth, G.K. (2014). voom: Precision weights unlock linear model analysis tools for RNA-seq read counts. Genome Biol. *15*, R29. https://doi.org/10.1186/gb-2014-15-2-r29.

STAR★METHODS

KEY RESOURCES TABLE

REAGENT or RESOURCE	SOURCE	IDENTIFIER
Antibodies		
Rabbit monoclonal anti-TTF1	Abcam	Cat#ab76013; RRID:AB_1310784
Mouse monoclonal anti-Hop Antibody (E-1)	Santa Cruz Biotechnology	Cat#sc-398703; RRID:AB_2687966
Rabbit polyclonal anti-SFTPC	Invitrogen	Cat#PA5-102493; RRID: AB_2851895
Mouse monoclonal anti-RAGE	R&D	Cat#MAB1179; RRID:AB_2289349
Rabbit polyclonal anti-Sox9	Milipore	Cat# AB5535; RRID: AB_2239761
Rabbit monoclonal anti-Sox2	Cell Signaling Technology	Cat#23064; RRID: AB_2714146
Mouse polyclonal anti-ICAM-1	R&D	Cat# AF796; RRID: AB_2248703
Hamster monoclonal anti-PDPN	DSHB	Cat#8.1.1; RRID: AB_531893
Rabbit monoclonal anti- PDGFR alpha	Abcam	Cat# ab203491; RRID: AB_2892065
Goat polyclonal anti-CD31	R&D	Cat# AF3628; RRID: AB_2161028
Mouse monoclonal anti-acetylated Tubulin	Sigma	Cat# T7451;RRID: AB_609894
Mouse monoclonal anti-CC10(E-11)	Santa Cruz Biotechnology	Cat# sc365992; RRID: AB_10915481
Donkey polyclonal anti-rabbit IgG (H+L) (Alexa Fluor® 568)	Thermo Fisher	Cat# A10042; RRID: AB_2534017
Donkey polyclonal anti-goat IgG (H+L) (Alexa Fluor® 647)	Thermo Fisher	Cat# A-21447; RRID: AB_2535864
Donkey polyclonal anti-rat IgG (H+L) (Alexa Fluor® 568)	Thermo Fisher	Cat# A78946; RRID: AB_2910653
Goat polyclonal anti- hamster IgG (H+L) (Alexa Fluor® 647)	Thermo Fisher	Cat#A21451; RRID: AB_2535868
Donkey polyclonal anti-mouse IgG (H+L) (Alexa Fluor® 488)	Thermo Fisher	Cat#A21202; RRID: AB_141607
Donkey polyclonal anti-mouse IgG (H+L) (Alexa Fluor® 568)	Thermo Fisher	Cat#A10037; RRID: AB_11180865
Donkey polyclonal anti-rabbit IgG (H+L) (Alexa Fluor® 488)	Thermo Fisher	Cat#A21206; RRID: AB_2535792
Goat polyclonal anti-rat IgG (H+L) (Alexa Fluor® 647)	Thermo Fisher	Cat#A21247; RRID: AB_141778
Biological samples		
Mouse lung	This paper	N/A
Chemicals, peptides, and recombinant proteins		
Dispase II	Gibco	Cat#17105-041
Matrigel	Corning	Cat#354234
DMEM/F12	Gibco	Cat#11330032
N2 supplement	Gibco	Cat#17502-048
B27	Gibco	Cat#17504-044
Penicilin-Streptomycin	Gibco	Cat#15140-122
CHIR99021	Targetmol	Cat#T2310;
FGF7	R&D	Cat#251
FGF10	Peprotech	Cat#100-26
BMP4	R&D	Cat# 314-BP
TGF-β1	Peprotech	Cat#100-21
SHH	R&D	Cat# 464-SH
Roxadustat	Selleck	Cat#S1007;
Vitamin C	Sigma	Cat#49752
Monothioglycerol	Sigma	Cat#M6145
EPZ5676	Targetmol	Cat#T3099;
RA	MCE	Cat# HY-14649;
EGF	R&D	Cat#2028-EG-200
Bleomycin sulfate	Macklin	Cat#B802467;
Papain	Worthington	Cat#LS003126
BSA	Miltenyi Biotec	Cat#130-091-376

(*Continued on next page*)

Continued

REAGENT or RESOURCE	SOURCE	IDENTIFIER
TRIzol Reagent	Invitrogen	Cat#TR118
fetal bovine serum	NTC	Cat#SFBE
Liberase TM	Roche	Cat#LIBTM-RO
DNase I	Worthington Biochemicals	Cat#LS006343
ACK lysing buffer	ThermoFisher	Cat#A1049201
4% paraformaldehyde	Coolaber	Cat#SL1830
sucrose solutions	Macklin	Cat#:C17413261;
OCT	Sakura	Cat#4583
TritonX-100	Yeasen	Cat#20107ES20;
PBS	Cytiva	Cat#SH30256.01
SPY-555-FastActTM	Cytoskeleton	Cat#SC205
DAPI	Invitrogen	Cat#D1306
Critical commercial assays		
Chromium Next GEM Single Cell 3′ GEM, Library & Gel Bead Kit v3.1	10X Genomics	Cat#PN-1000121
VAHTS mRNA-seq v2 Library Prep Kit for Illumina	Vazyme	Cat#NR605
Masson's trichrome staining kit	Solarbio	Cat# G1346
Deposited data		
RNA sequencing data (raw and analyzed data)	This paper	GSE303739
scRNAseq sequencing data (raw and analyzed data)	This paper	GSE303739
Public scRNA-seq data	Negretti et al.[46]	GSE165063
Public scRNA-seq data	Zepp et al.[47]	GSE149563
Public scRNA-seq data	Strunz et al.[48]	GSE141259
Public scRNA-seq data	Angelidis et al.[49]	GSE124872
Experimental models: Organisms/strains		
Mouse: C57/6J Rosa26-mTmG	The Jackson Laboratory	RRID:IMSR_JAX007576
Mouse: CD-1®(ICR) IGS	Guangdong Vital River Laboratory Animal Technology Co., Ltd.	No.201
Mouse: C57BL/6J	GemPharmatech Co., Ltd.	No. N000013
Software and algorithms		
Napari(v0.5.4)	N/A	https://www.python.org/
Fiji	Schneider et al.[51]	https://imagej.net/software/fiji/
Networkx(v3.4.2)	Hagberg and Conway[52]	https://github.com/networkx/networkx
Umap-learn(v0.5.7)	McInnes et al.[53]	https://umap-learn.readthedocs.io/en/latest/
micro-SAM(v1.3.1)	Archit et al.[54]	https://github.com/computational-cell-analytics/micro-sam
Matplotlib(v3.1.0)	Hunter et al.[55]	https://matplotlib.org/stable/
FlowJo (v10.8.1)	BD Biosciences	N/A
Bowtie2	N/A	http://bowtie-bio.sourceforge.net/bowtie2/index.shtml
RSEM	N/A	https://github.com/deweylab/RSEM
STAR (v2.7.6a)	N/A	https://github.com/alexdobin/STAR
R (v4.2.2)	R Core Team	https://www.r-project.org/
ggplot2 (v3.3.2)	N/A	https://github.com/tidyverse/ggplot2
Seurat (v4.3.0)	N/A	http://www.satijalab.org/seurat
Python (v3.11)	Python Software Foundation	https://www.python.org/
Scanpy (v1.9.6)	N/A	https://scanpy.readthedocs.io/en/stable/
scVI (v1.4.1)	N/A	https://scvi-tools.org/

(*Continued on next page*)

Continued

REAGENT or RESOURCE	SOURCE	IDENTIFIER
Palantir (v1.4.2)	N/A	https://palantir.readthedocs.io/en/latest/notebooks/Palantir_sample_notebook.html
CellRank (v2.0.7)	N/A	https://cellrank.readthedocs.io/en/latest/notebooks/tutorials/index.html
Matlab (vR2023a)	N/A	https://matlab.mathworks.com/
ZEN 2.3 SP1	Zeiss	N/A

EXPERIMENTAL MODEL AND STUDY PARTICIPANT DETAILS

Animals

All animal experiments were performed in accordance with the Guide for the Animal Use and Care Protocol (AUCP, GZLAB-AUCP-2024-10-A03) and approved by the Animal Ethics Committee of Guangzhou Laboratory. Mice were housed with a 12-hlight-dark cycle at 18-23°C and 40-60% humidity in the animal facility at Guangzhou Laboratory. Wild-type ICR and C57BL/6 mice were purchased from Charles River Laboratories, SCXK (Yue) 2022-0063. Rosa26-mTmG (C57BL/6J background) mice (gifts from Qi Chen lab). Wild-type pregnant female ICR and C57BL/6 mice (8-10 weeks old) were used for embryonic lung isolation. Male C57BL/6J mice (8-10 weeks old) were subjected to a bleomycin (BLM)-induced fibrotic injury model.

Organoid culture

Branching lung organoids (BLOs) derived from mouse embryonic lung tip epithelium were cultured in the medium consisting of DMEM/F12 (Gibco, #11330032) supplemented with 1% N2 supplement (Gibco, #17502-048), 2% B27 supplement (Gibco, #17504-044), and 1% penicillin–streptomycin (Gibco, #15140-122), 3 μM CHIR99021 (Targetmol,T2310) and 10 ng/ml FGF7(R&D, #251), 0.4 mM monothioglycerol (Sigma, #M6145), 50 ug/ml vitamin C (Sigma, #49752), and 10 ng/ml FGF10 (Peprotech, #100-26).

METHOD DETAILS

Isolation and microdissection of mouse embryonic lung distal tip epithelium for BLO induction

Timed pregnancies were established in ICR or Rosa26-mTmG C57BL/6 mice, with the morning of vaginal plug detection designated as embryonic day 0.5 (E0.5). Pregnant females were euthanized at embryonic days E9.5 to E18.0, and embryos were harvested. After sterilization of the abdominal surface with 75% ethanol, uterine horns were excised and embryos were isolated under a stereomicroscope. Embryonic lungs at the indicated developmental stages were carefully dissected and incubated in 10 U/mL Dispase II (Gibco, #17105-041) for 5–10 min to facilitate separation of epithelial and mesenchymal compartments. Following enzymatic digestion, the mesenchyme was gently removed by mechanical dissection under a stereomicroscope, yielding purified lung epithelial tissues.

The procedure for harvesting epithelial starting material was adapted according to developmental stage and tissue morphology:

E9.5 embryos: At this stage, the laryngotracheal groove has just emerged ventrally from the foregut and initiated bifurcation. The entire nascent lung bud was isolated and processed as described above to obtain primordial lung epithelium for culture.

E10.5–E16.5 embryos (pseudoglandular stage): After mesenchymal removal, the most distal epithelial tip regions of the lung buds were precisely microdissected using an insulin syringe needle (BD, #328421) or further mechanically dissociated into smaller epithelial clusters using tungsten needles (F.S.T., #10130-05) for organoid culture.

Embryos beyond E16.5 (canalicular and saccular stages): Following mesenchymal removal, terminal epithelial clusters were similarly microdissected using an insulin syringe needle and used for organoid culture.

Culture medium formulation for BLO induction

Isolated distal tip epithelium or terminal epithelial clusters were embedded in 50 μL droplets of Matrigel (Corning, #354234) and placed at the center of each well in a 24-well plate. After Matrigel polymerization, the appropriate culture medium was added to each well. Cultures were maintained at 37 °C in a humidified incubator with 5% CO_2, and the medium was refreshed every 48 h.

The basal medium used for all experiments consisted of DMEM/F12 (Gibco, #11330032) supplemented with 1% N2 supplement (Gibco, #17502-048), 2% B27 supplement (Gibco, #17504-044), and 1% penicillin–streptomycin (Gibco, #15140-122).

For specific experimental conditions, the basal medium was further supplemented as follows:

Initial screening conditions: The basal medium was individually supplemented with candidate small molecules or growth factors. A complete list of all screened factors, including catalog numbers and working concentrations, is provided in Table S1.

2C condition (2C medium): The basal medium was supplemented with CHIR99021 and FGF7.

Final optimized condition (ALL medium): The basal medium was supplemented with the 2C combination together with three additional components: monothioglycerol (MTG), vitamin C (Vc), and FGF10.

Withdrawal assay conditions: Modified versions of the ALL medium were generated by omitting a single small molecule, including ALL–Vc, ALL–MTG, ALL–FGF10, ALL–CHIR99021, and ALL–FGF7.

Assessment of branching-inducing capacity of lung tip epithelium

The branching-inducing capacity of lung tip epithelium was evaluated primarily based on characteristic morphological progression observed during daily monitoring of organoid cultures. The criteria were defined as follows:

(1) Sustained proliferation: lung tip /distal epithelial cluster exhibited robust growth during the early culture period, characterized by a continuous increase in organoid volume and the persistent generation of new branches up to day 8.
(2) Hierarchical branch formation: Primary (first-order) branches emerged within the first 4 days, followed by the sequential appearance of secondary and higher-order branches. By day 8, organoids established a well-organized dendritic architecture.
(3) Diversity of branching modes: Individual organoids displayed multiple branching modalities characteristic of in vivo lung development, including domain branching, planar bifurcation, and orthogonal bifurcation.
(4) Core scaffold with peripheral elaboration: Mature organoids developed a central dendritic scaffold that served as a structural framework for continued morphogenesis, including further branch extension and differentiation of distal termini into sac-like structures.

Live-cell imaging

Live-cell imaging of branching lung organoids (BLOs) was performed using organoids generated as described above. Briefly, isolated E10.5 lung tip epithelium was embedded in Matrigel and plated into glass-bottom 24-well plates (Cellvis, P24-1.5H-N) for time-lapse imaging. Organoids were imaged on an inverted microscope (Eclipse Ti2-E, Nikon) equipped with a 10×/0.45 NA objective. A Spectra X light engine (Lumencor) was used for fluorescence imaging and the exposure time for each channel was 200 ms. The full field of view was recorded every 10 min for approximately 5 days. During imaging, cultures were maintained in an OKO live-cell incubation chamber under a humidified atmosphere at 37 °C with 5% CO_2. For image analysis, The mask of recorded date was extracted with the napari plugin micro-SAM, which is based on the Segment Anything Model (SAM).[54] Morphological quantification and dynamic analysis of organoid growth and branching behavior were subsequently performed by a customized Matab script.

BLOs skeletonization analysis

The recoded 3D image stack of the BLOs at Day5 was segmented using Labkit plugin of Fiji to generate mask. The raw mask would be carefully checked and manually corrected if any error was found. A spline smoothing algorithm was performed on each image slice to get smooth 2D boundaries. For smoothing in 3D, the mask was converted into a stl file using ''3D Viewer'' plugin of Fiji and then imported to the software of Meshlab. Laplacian Smooth and down-sampling were used to get a smooth 3D surface. After converting the smoothed mask into an image stack, a customized Fiji script would skeletonize the mask image and convert the skeleton into a tree structure which stores in a JSON or HDF5 file.

The mouse airway data were downloaded from the National Toxicology Program of U.S Department of Health and Human Services (https://cebs-ext.niehs.nih.gov/cahs/report/lapd/web-download-links).The human airway data were downloaded from a Pulmonary-Tree-Repairing project (https://github.com/m3dv/pulmonary-tree-repairing?tab=readme-ov-file). The mouse salivary gland data were gathered from the paper ''Inflationary theory of branching morphogenesis in the mouse salivary gland (2022)''[56].

Branching tree similarity analysis

We invented a method named branching kernel composition vector (BKCV) to do the branching tree similarity analysis. Firstly, the branching tree was checked and modified (if necessary) into a binary branching tree by merging nodes with only one child and splitting nodes with more than 3 children. Next, all nodes except root and leaf nodes would be classified into one of the two commonsensical branching types: budding (or branching) and clefting (or bifurcation). These two branching types were defined as level-1 (L1) branching kernels. The criteria we used to classify L1 kernel are detailed in Figure S3C Level-2 (L2) kernel is defined as two connected L1 kernels. Considering the spatial configuration, the connection was further subdivided into a 2D version (the dihedral angle of the two planes defined by the connected nodes is smaller than 30°) or a 3D version (the dihedral angle is bigger than 30°). After emulating all the possible non-isomorphic L2 kernels, a branching tree kernel atlas had been constructed (Figure 4G). Of note, one can construct a kernel atlas based on the problem one is interested in, such as degenerating some branching kernels we listed or adding the length of the connecting edge as extra parameter to gain more kernels. For any given branching tree, one can count the number of all different L2 kernels. The percentage composition of each type of kernel is obtained by dividing its number by the total number of L2 kernels. The collection of all type kernels' percentage is the BKCV.

The Uniform Manifold Approximation & Projection (UMAP) was used to do the dimension reduction of all BKCVs. Considering the BKCV is percentage composition, the change of BKCV will be much less when adding same amount nodes into a tree with more nodes than a tree with less nodes. So we used the distance metric of Canberra ($d_{\text{Canberra}} = \sum_1^n \frac{|x_i - y_i|}{|x_i + y_i|}$, for $\mathbf{x} = [x_1, x_2, \ldots, x_n]$ *and* $\boldsymbol{y} = [y_1, y_2, \ldots, y_n]$) instead of Euclidean during UMAP calculation for balancing the node number difference effect. To mimic the data of different mouse airway development stages, the adult mouse airway trees were pruned the thinnest branch sequentially till certain number of nodes left: 1200 (Mouse Airway-P1), 800 (Mouse Airway-P2), 500 (Mouse Airway-P3), 200 (Mouse Airway-P4) and

50 (Mouse Airway-P5) nodes (Figure S5D). For human airway, the pruning process was similar. The Human Airway-P1 left 150 nodes, Human Airway-P2 and P3 left 100 and 50 nodes, respectively. The putative mouse airway development trace in UMAP was obtained by linking the data center sequentially from Mouse Airway-P1 to Mouse Airway-P5.

Bleomycin-induced lung injury model and cell transplantation

Bleomycin injury model

Bleomycin (BLM) was freshly prepared in sterile saline at a stock concentration of 25 mg/mL and stored at −80 °C. Immediately before use, the stock solution was diluted to 0.5 mg/mL with sterile saline. Seven days prior to cell transplantation (day−7), male C57BL/6 mice (9–10 weeks old) received a single intratracheal instillation of BLM at a dose of 1 mg/kg body weight. Control (sham) mice were administered an equivalent volume of sterile PBS via the same route.

Preparation of donor cells

BLOs were generated from E10.5 or E12.5 embryos of Rosa26-mTmG reporter mice on a C57BL/6 background. Organoids were cultured to the indicated stages prior to transplantation (E10.5-derived BLOs: day 11 or day 18; E12.5-derived BLOs: day 10). For cell dissociation, organoids were gently released from Matrigel and enzymatically digested with papain at 37 °C for 10 min to generate single-cell suspensions. Cells were washed in 0.04% bovine serum albumin (BSA), passed through a 100 μm cell strainer to remove aggregates, and resuspended in culture medium at a final concentration of 1.2×10^7 cells/mL.

Transplantation procedure

On day 0, BLM-injured mice received an intratracheal injection of 6×10^5 donor cells in a total volume of 50 μL of culture medium. Donor cells were derived from mTmG-positive organoids, allowing in vivo tracking by constitutive membrane-targeted mtdTomato fluorescence.

Tissue harvest and imaging

At 21 days post-transplantation (dpt), mice were euthanized and lungs were perfused with PBS. Whole lungs were then explanted and imaged ex vivo using a stereomicroscope (Zeiss Axio Zoom.V16) to assess the gross distribution and engraftment of mtdTomato-positive donor cells.

Measurement of mouse lung function

At 21 days post-transplantation, pulmonary function was assessed in three experimental groups: PBS sham-operated control (N = 5); BLM-injured control (N = 5); and BLM-injured mice transplanted with mtdTomato-positive cells from BLOs (N = 6).

Mice were weighed and anesthetized with an intraperitoneal injection of Avertin to ensure adequate sedation for the procedure. Once a sufficient depth of anesthesia was confirmed, a midline incision was made in the neck skin using surgical scissors, and the connective tissue surrounding the trachea was carefully blunt-dissected with forceps to expose the trachea. A small incision (approximately 1 mm) was then made in the trachea, into which a tracheal cannula was inserted and secured with a cotton thread.

Following cannulation, each mouse was connected via the endotracheal cannula to a small animal pulmonary function testing system (PFT, DSI Buxco). Pulmonary function parameters, including vital capacity (VC), forced vital capacity (FVC), airway resistance (RI), quasi-static lung compliance (Cchord), and dynamic lung compliance (Cdyn), were assessed using standardized measurement protocols. Data acquisition, analysis, and result generation were performed using the FinePointe software system, ensuring precise and reproducible evaluation of lung function in mice.

Small-animal micro-computed tomography (micro-CT)

Lung morphology was assessed and compared among BLM-injured control mice and BLM-injured mice that received BLOs-derived cell transplantation at 21 or 180 dpt. Mice were anesthetized by intraperitoneal injection of Avertin to ensure immobilization during image acquisition. Micro-CT scans were performed using a PerkinElmer small-animal micro-CT system. Images were acquired with a field of view ranging from 1 to 8 cm and a tunable spatial resolution between 5 and 200 μm, achieving a maximal resolution of 2.3 μm. The scan speed was set to 3.9 s per rotation, with a minimum radiation dose of 5 mGy. The total acquisition time was approximately 4 min per mouse. All projection data were reconstructed using the system's control panel software and further processed with Quantum GX Basic Analysis Software to generate digital images for subsequent analysis.

Bulk RNA library preparation and sequencing

Total RNA was extracted from BLOs using TRIzol Reagent (Invitrogen, TR118) following the manufacturer instructions. Subsequently, sequencing libraries were constructed using the VAHTS mRNA-seq v2 Library Prep Kit for Illumina (NR605, Vazyme). Library sequencing was performed on an Illumina NovaSeq X Plus platform (ANNOROAD GENE TECHNOLOGY).

Single-cell RNA library preparation and sequencing

Organoids were carefully separated from Matrigel using insulin syringe needles (BD, #328421) and enzymatically dissociated into single cells by incubating with 10 U/mL Papain (Worthington, LS003126) at 37 °C for 20 minutes. Digestion was terminated by adding an equal volume of 10% fetal bovine serum (FBS, NTC, #SFBE). The resulting cell suspension was filtered through a 40-μm strainer (Falcon, 352340) and centrifuged at 300× g for 5 min at 4 °C. Then cell pellet was then resuspended in PBS containing 0.04% BSA (Miltenyi Biotec, #130-091-376) and adjusted to a final concentration of 1×10^6 cells/mL. For single-cell RNA sequencing library construction, single cells from each sample were loaded onto the Chromium Single Cell 3′ Kit v3.1 (10× Genomics) / the 10× Genomics

Chromium platform (v3.1 chemistry) to generate single-cell gel beads-in-emulsion (GEMs), enabling barcoding of full-length cDNA from individual cells. Following incubation, GEMs were disrupted, and cDNA was amplified by PCR. Single-cell 3‘ gene expression libraries were constructed using 10 μL of amplified cDNA and purified with SPRIselect beads. Library quality and fragment size distribution were assessed using a Qsep 100 system, and concentrations were quantified by Qubit 4.0 fluorometer. Finally, libraries were sequenced on an Illumina Novaseq X Plus platform (ANNOROAD GENE TECHNOLOGY). BLOs samples prepared for Single-cell RNA-seq were listed in Table S2.

Flow cytometric sorting and scRNA-seq of post-transplant lung tissues

Lung tissues were harvested at 28, 90, and 180 dpt from mice that received transplants of mtdTomato-positive BLO-derived cells. Excised lungs were finely minced and enzymatically dissociated in a digestion cocktail containing 1.25 mg/mL Liberase TM (Roche, LIBTM-RO) and 100 U/mL DNase I (Worthington Biochemicals, LS006343) at 37 °C for 30 min in a water bath. The resulting single-cell suspension was filtered through a 100 μm cell strainer (Falcon, 352360) to remove undigested tissue fragments, followed by red blood cell lysis using ACK lysing buffer (ThermoFisher, A1049201).

Wild-type lung cells were used as negative controls to establish gating parameters for fluorescence-based sorting. Engrafted donor-derived cells were identified by constitutive mtdTomato fluorescence and sorted into mtdTomato-positive and mtdTomato-negative populations using a BD FACS Aria Fusion flow cytometer. Sorted cells were immediately processed for single-cell RNA-seq library preparation using the 10x Genomics Chromium platform, following the same procedures described above for scRNA-seq analysis of BLOs. Generated libraries were sequenced and analyzed to characterize the transcriptional profiles of engrafted donor cells and host lung cell populations at different post-transplantation time points.

Bulk RNA-seq data analysis

Following sequencing, paired-end reads were aligned to a transcriptome index generated from GENCODE mm10 annotations using Bowtie2[57] and RSEM.[58] Gene expression levels were quantified as both raw counts and Transcripts Per Kilobase Million (TPM). The raw count matrix served as the input for downstream differential expression analysis conducted using DESeq2[59] within the R/Bioconductor environment (v3.16).[60] To capture gene expression variability, the top 5,000 highly variable genes were identified and used for principal component analysis (PCA) and correlation analysis. Dynamic gene expression patterns during the tip organoid induction process were further explored using Mfuzz clustering.[61] Functional enrichment of differentially expressed genes was assessed via Gene Ontology (GO) analysis using the R package clusterProfiler,[62] applying a significance threshold of $p < 0.05$. All statistical analyses and data visualizations were performed in R(v4.2.2), with plots generated using ggplot2 (v3.3.2).[63]

Single-cell RNA-seq analysis of BLOs

Data Processing, Cell Filtering and Clustering

Raw data quality assessment was performed using FastQC. FASTQ files were aligned to the mouse genome (mm10) using the STARsolo module of STAR (v2.7.6a).[64] Data processing was carried out with Scanpy (v1.9.6),[65] retaining cells with UMI counts < 80,000, detected gene numbers between 1,000-9,000, and mitochondrial gene percentage <20% for subsequent analysis. Doublets were identified and removed using Scrublet.[66] A total of 57,150 high-quality cells were retained after filtering. All data were normalized using ‘scanpy.pp.normalize_total’ followed by log-transformation by ‘scanpy.pp.log1p’. Highly variable genes (HVGs) were identified using ‘scanpy.pp.highly_variable_genes’.

Data Integration and Latent Representation

To mitigate technical biases across sampling timepoints and experimental batches, we employed a deep generative modeling framework for data integration. Specifically, scVI (v1.4.1)[67] was utilized to model the raw count matrix through variational inference. Subsequently, the scANVI (single-cell annotation-trained Variational Inference) module[68] was implemented for semi-supervised learning, incorporating preliminary cell-type annotations to achieve a biologically refined low-dimensional latent embedding (X_scANVI). This latent space served as the foundation for downstream dimensionality reduction, manifold learning, and trajectory inference. Global cell distributions were visualized using UMAP.[69]

Lineage Partitioning and Trajectory Reconstruction

Datasets were partitioned into proximal and distal lineages based on anatomical and functional markers. In the X_scANVI latent space, k-nearest neighbor (k-NN) graphs were constructed (k=30–50). For the proximal lineage, cell-type-based downsampling (capped at 5,000 cells per group) was applied to prevent high-abundance populations from biasing the trajectory. Diffusion Maps[70] were employed to capture continuous transitions in cellular states. Specific Diffusion Components (DCs) were selected for optimized projection to best capture biologically relevant transitions, such as alveolar differentiation in the distal lineage and branching morphogenesis in the proximal lineage, while excluding components representing confounding technical variation.

Pseudotime Modeling and Dynamics Inference. The developmental root was defined by searching for extrema within the diffusion embedding among cells sampled at E10.5 Tip. Based on this root, Diffusion Pseudotime (DPT) was calculated to measure local continuity, while Palantir (v1.4.2)[71] was used to estimate differentiation entropy. Directional trajectories were reconstructed using the CellRank (v2.0.7)[72] framework. A PseudotimeKernel was constructed to compute transition probabilities based on DPT gradients. Differentiation flows were visualized as streamlines projected onto the UMAP space, with background shading representing Palantir pseudotime.

Strain and Source Conservation Analysis

To evaluate the robustness of BLO differentiation across varying progenitor sources and genetic backgrounds, we performed an integrated analysis of BLOs initiated from different embryonic days (E10.5, E11.5, and E12.5) and mouse strains (C57BL/6). Samples collected at comparable differentiation stages (Day 9-11) were integrated using the Harmony (v0.0.10)[73] algorithm within the Scanpy environment to mitigate source-specific batch effects while preserving biological variation. The resulting integrated manifold was visualized via UMAP to assess the convergence of cell-type identities and the conservation of differentiation programs across diverse initial developmental states and genetic backgrounds.

Integrated analysis of multiple datasets

Data Preprocessing

A natural developing lung (NDL) atlas, comprising 7,434 high-quality cells, was used as a reference. Cells were filtered based on UMI counts (<150,000), gene features (1,000–11,000), and mitochondrial content (<20%). Clusters were annotated using canonical lung markers (Figure S3B). To mitigate potential bias driven by overrepresented cell types and ensure balanced lineage representation during integration, the BLOs dataset was downsampled to a maximum of 300 cells per cluster.

Reference-based Integration

Datasets were independently normalized using Seurat (v4.3.0) SCTransform,[74] and 3,000 highly variable genes (HVGs) were selected. We utilized Canonical Correlation Analysis (CCA) to identify Mutual Nearest Neighbor (MNN) anchors,[75] effectively mitigating batch effects between the in vitro culture (BLOs) and in vivo tissue (NDL). The resulting joint embedding validated that in vitro lineages converged with their in vivo counterparts.

Topology and Visualization

The integrated Seurat object was converted via dior/diopy[76] for analysis in Scanpy. A KNN graph was constructed using the top 20 PCs. We employed Partition-based Graph Abstraction (PAGA)[77] to resolve developmental connectivity, and the final manifold was visualized using a ForceAtlas2 layout,[78] color-coded by cell type.

Transcriptomic Similarity

We further evaluated the similarity between BLOs and natural lung cell states via cluster-level correlation analysis in Scanpy. Hierarchical clustering 'sc.tl.dendrogram' and correlation matrices 'sc.pl.correlation_matrix' were computed based on averaged expression profiles to quantify the transcriptomic alignment across developmental stages.

Maturity Evaluation

To assess the developmental maturity of BLOs, we compared them against the epithelial lineages of longitudinal mouse lung development atlas spanning E9.5 to postnatal 24 months, integrated from multiple publicly available datasets. Single-cell RNA-seq data were aggregated into pseudo-bulk expression matrices by summing counts across all epithelial cells for each developmental stage. Data normalization was performed using limma-voom,[79] and global transcriptomic similarities were evaluated via Principal Component Analysis (PCA).

ScRNA-seq analysis of post-transplant lung tissue

Paired-end sequencing reads were aligned to mm10 genome (appended with tdTomato sequences) using the cellranger (v6.1.1). Data preprocessing was performed with Python library Scanpy (v1.6.0). Low-quality cells were filtered out based on the following criteria: less than 1,000 and greater than 6,000 detected genes, the sum of UMI counts exceeding 30,000, and mitochondrial gene percentage greater than 10%. After filtering, 25976 cells were retained from the endogenous samples, and 23843 cells from the donor-derived samples. The HVGs were conducted for PCA and then found the neighbors for each cell with 30 PCs. UMAP was used for dimensionality reduction and visualization. Leiden clustering was processed on the HVGs calculated across each sample. Cell annotation was performed on these samples at 28, 90, and 180 dpt respectively, with marker genes associated with each cluster. Epithelial cells were subsequently selected for re-dimensionality reduction analysis.

Histopathological analysis

For histopathological analysis, the lung tissue samples were fixed overnight at 4 °C in 4% paraformaldehyde (PFA, Coolaber, SL1830-500 mL), followed by graded dehydration in sucrose (Macklin, #57-50-1) solutions of increasing concentrations (10%, 20%, 30%). The tissues were then embedded in OCT (Sakura, #4583) compound and sectioned at a thickness of 10μm using a cryostat (Leica, CM 3050 S). Sections were mounted on poly-lysine-coated glass slides (Citotest, #188105) and stored at 4°C until further processing for immunostaining or histopathological analysis. Hematoxylin and eosin (H&E) staining (Kit, Solarbio, G1121) and Masson's trichrome staining (Kit, Solarbio, G1346) were performed according to standard protocols. Regions of interest in each section were identified and delineated using a Digital Pathology Scanner (Leica Aperio CS2).

Immunostaining

Cultured branching lung organoids were fixed in 4% paraformaldehyde (PFA) for 30 min and followed by overnight dehydration in 30% sucrose at 4°C. The organoids were then embedded in OCT (Sakura, #4583) compound and cryosectioned at a thickness of 10 um. Sections were mounted on poly-lysine-coated glass slides and stored at 4°C until further processing.

For immunostaining, BLO and lung tissue sample section slides washed three times with PBS, permeabilized with 0.5% TritonX-100 for 20 min, and subsequently blocked with blocking buffer (5% BSA in PBS) at room temperature for 1 hour. The sections were

then incubated overnight at 4 °C with the following primary antibodies were used: NKX2-1 (1:200, Abcam, ab76013), HOPX (1:50, Santa Cruz, sc398703), SFTPC (1:400, Invitrogen, PA5-102493), RAGE (1:800, R&D, MAB1179), SOX9 (1:200, Milipore, AB5535), SOX2 (1:200. Cell Signaling Technology, #23064), ICAM1 (1:100, R&D, AF796), PDPN (1:50, DSHB, #8.1.1), PDGFRα (1:500, Abcam, ab203491), CD31/PECAM-1 (1:100, R&D, AF3628), ACTUB (1:500, Sigma, T7451), CC10 (1:50, Santa Cruz, sc365992). The next day, slides were washed three times with PBS for 10 min each, followed by incubation with Alexa Fluor-conjugated Donkey or Goat anti-mouse/rabbit/rat/goat/hamster secondary antibodies (488/568/647, 1:500, Thermo Fisher) at room temperature for 2 hours. After secondary antibody incubation, slides were washed three times with PBS (10 min per wash), and nuclei were stained with DAPI (Invitrogen, D1306) for 10 min. Finally, slides were washed twice with PBS and mounted using appropriate mounting media (KeyGEN BioTECH, KGA1523-5). Imaging was performed using either Andor Dragonfly 200 or Olympus IXplore SpinSR confocal microscope. Antibodies used for staining are detailed in the key resources table.

Whole-mount immunostaining and live-cell staining

For whole-mount immunostaining, organoids were fixed in 4% PFA for 1 hour, followed by three washes with PBS. Samples were then incubated with blocking buffer at 4 °C overnight. The next day, primary antibodies: NKX2-1 (1:200, Abcam, ab76013), HOPX (1:50, Santa Cruz, sc398703), SFTPC (1:400, Invitrogen, PA5-102493), RAGE (1:800, R&D, MAB1179), SOX9 (1:200, Milipore, AB5535), SOX2 (1:200. Cell Signaling Technology, #23064), ICAM1 (1:100, R&D, AF796) were incubated at 4 °C for 3 days. After primary antibodies incubation, samples were washed three times with PBST (0.05% Tween-20 in PBS), each wash lasting 1 hour. Alexa-conjugated donkey or goat secondary antibodies (488/568/647, 1:500, Thermo Fisher) were then applied for 2 days at 4°C. This was followed by three additional 1 hours washes with PBST. Nuclei were counterstained with DAPI for 30 minutes. For live-cell F-actin labelling, the fluorescent dye SPY-555-FastActTM (Cytoskeleton, SC205) was diluted 1:1000 in lung branching organoids medium and incubated for 24 hours, allowing for the visualization of red fluorescence in live organoid cells. For both whole-mount imaging, multi-layer (z-stack) and large field images were acquired using either Andor Dragonfly 200 or Olympus IXplore SpinSR confocal microscope. Antibodies used for staining are detailed in the key resources table.

QUANTIFICATION AND STATISTICAL ANALYSES

Statistical analysis

Statistical analyses were performed using MATLAB. Details regarding the number of biological replicates, the specific statistical tests applied, and the exact P values used to determine statistical significance are provided in the corresponding figure legends.

Software

In addition to the aforementioned software/plugins, the following tools were utilized: The Kappa plugin in FIJI[51] was used to quantify curvature and fluorescence intensity along curved ROIs. Wide-field data masks were generated using the "micro-SAM"[54] plugin in Napari, which implements the Segment Anything Model (SAM). Mask morphology quantification was done by a custom MATLAB script. 3D volume rendering was performed in Napari. A custom Python module (based on NetworkX) processed graph/tree structures. Dimensionality reduction using UMAP[53] was computed via Python's umap-learn package. Figures were created using MATLAB or Python's Matplotlib.[55]